NATIONAL AERONAUTICS AND SPACE ADMINISTRATION

Technical Memorandum No. 33-237

Use of Ranger Flight Data in the Synthesis of a Torsional Acceleration Transient for Surveyor Vibration Qualification Testing

Marc R. Trubert

JET PROPULSION LABORATORY
CALIFORNIA INSTITUTE OF TECHNOLOGY
PASADENA, CALIFORNIA

April 19, 1966

NATIONAL AERONAUTICS AND SPACE ADMINISTRATION

Technical Memorandum No. 33-237

Use of Ranger Flight Data in the Synthesis of a Torsional Acceleration Transient for Surveyor Vibration Qualification Testing

Marc R. Trubert

M. E. Alper

M. E. Alper, *Manager*
Applied Mechanics Section

JET PROPULSION LABORATORY
CALIFORNIA INSTITUTE OF TECHNOLOGY
PASADENA, CALIFORNIA

April 19, 1966

Prepared Under Contract No. NAS 7-100
National Aeronautics & Space Administration

CONTENTS

TABLES

FIGURES

FIGURES (Cont'd)

ABSTRACT

This Technical Memorandum presents a method for the prediction of the flight acceleration at the base of a spacecraft in boost configuration from the flight data of another spacecraft using the same first-stage booster. The predicted acceleration furnishes a rational basis for the vibration specifications of the spacecraft. The method is illustrated with the torsional acceleration of the *Ranger* and *Surveyor* spacecraft. The study was made in three steps: In Step I, the pulsating transient acceleration, recorded at the base of *Ranger* during Flights *VI* through *IX* (booster engine cutoff event), was analyzed. A pulse type torque at the gimbal blocks of the *Atlas* engine was assumed to be cause of the transient acceleration and was determined on an analog computer. In Step II, this torque was applied on an analog model of the *Atlas/Centaur/Surveyor* vehicle; the corresponding acceleration at the base of *Surveyor* was deduced. In Step III, the attention was focused on the implementation of the pulse test program. In addition, recommendation for a sine sweep test was made by deriving a sine level that is equivalent to the pulses.

I. INTRODUCTION

This Technical Memorandum describes the method followed for the prediction of the flight transient torsional acceleration at the base of the *Surveyor* spacecraft and the later implementation of the vibration qualification testing. Basically, the method uses the data recorded during the boosted flights of the *Ranger* series, which exhibited a strong vibration transient at booster engine cutoff (BECO). This flight vibration was attributed to a disturbance associated with thrust decay, and manifested mechanically at the *Atlas* booster engine gimbal blocks. Because both spacecraft (*Ranger* and *Surveyor*) use essentially the same *Atlas* booster configuration, it was assumed that the same character of disturbance would occur for the *Surveyor* flight, inducing a torsional acceleration at the base of the spacecraft. The prediction of this acceleration, to be used for the specification of torsional vibration requirements of the *Surveyor* test model, is the first objective in this investigation. Then the analysis was pursued to determine a pilot pulse signal, which was used in the implementation of the pulse qualification test and permitted a determination of the sine wave level for the sine sweep qualification test requirement.

II. AVAILABLE DATA

The acceleration at several locations of the *Atlas/Agena/Ranger* vehicle was recorded for different events during the boosted flight of *Rangers VI* through *IX*. The most significant level of torsional acceleration occurred at BECO, the only event investigated here. Two different sets of data were available in the form of recorded acceleration time histories: the acceleration at the *Ranger* adapter and the acceleration at the gimbal blocks of the *Atlas* engine.

A tentative use of the acceleration at the gimbal blocks revealed that the results obtained from it, according to the method described later, were quite unrealistic. Several objections were advanced to reject the gimbal block flight acceleration as a useful source of data:

(1) The insufficiently refined mathematical model of the structure in the vicinity of the gimbal blocks, not accounting for local resonances.

(2) Cross-axis sensitivity of the accelerometers used.

(3) High-level noise environment effect on the accelerometer sensitivity.

On the contrary, the accelerometers located at the *Ranger* adapter were sufficiently far from the engine to be insentitive to the objections just mentioned; consequently, much confidence was placed in the flight acceleration at the *Ranger* adapter. This acceleration was used as input data for the problem at hand. Two accelerometers were placed at two opposite locations of the adapter in order to record, through telemetry, the tangential accelerations a_1 and a_2 on magnetic tape. Then these accelerations were properly combined on an analog computer at playback of the tape to produce the angular acceleration $\ddot{\theta}_1$ of the adapter in flight (Appendix A). This acceleration $\ddot{\theta}_1$ was recorded on magnetic tape and was the input data for the problem.

III. METHOD

It appeared legitimate to assume that the transient accelerations a_1 and a_2 (Appendix A) were due to a pulsating load applied at the gimbal blocks during the BECO event. Although the loading is undoubtedly complex in nature, the net effect at the *Ranger* adapter is unmistakably a torsional oscillation. The exact mechanism producing this torsional acceleration is not fully understood, but most likely results from a coupling between bending and torsion of the entire vehicle (Ref. 1). However, no mathematical model introducing this coupling had yet been developed; therefore, a simplified model accounting only for the torsion was considered (Ref. 2), and an equivalent unknown torque $T = T(t)$ at the gimbal blocks was assumed to be the cause of this acceleration. The sequence of the operations performed in the study is indicated in Fig. 1. In Step I, the unknown torque T is determined from the data obtained during the *Ranger* flights. In Step II, the torque T is then applied on the *Atlas/Centaur/Surveyor* vehicle, and the time history of the acceleration pulse at the *Surveyor* adapter is determined. In Step III, the pulse is simulated on the actual *Surveyor* spacecraft mounted on a shake table. Since the time histories of accelerations, torque, shaker voltage, etc., are eventually needed, an analog technique which gives directly those quantities in the form of electrical signals is best suited for the problem. However, the large number of degrees of freedom, one for each mass, introduced in the spring mass model precludes the sole use of the analog. Instead, a combination of analog and digital techniques is used, and the advantages of each technique are fully exploited.

First the digital technique, through the use of the standard eigenvalue program, permits a substantial reduction of the basic number of degrees of freedom to a small number of significant normal modes. Then the analog computer can use this reduced number of modes most advantageously to produce directly the desired time histories and to allow for any variation of parameters. Figure 2 shows a block diagram of the analog setup.

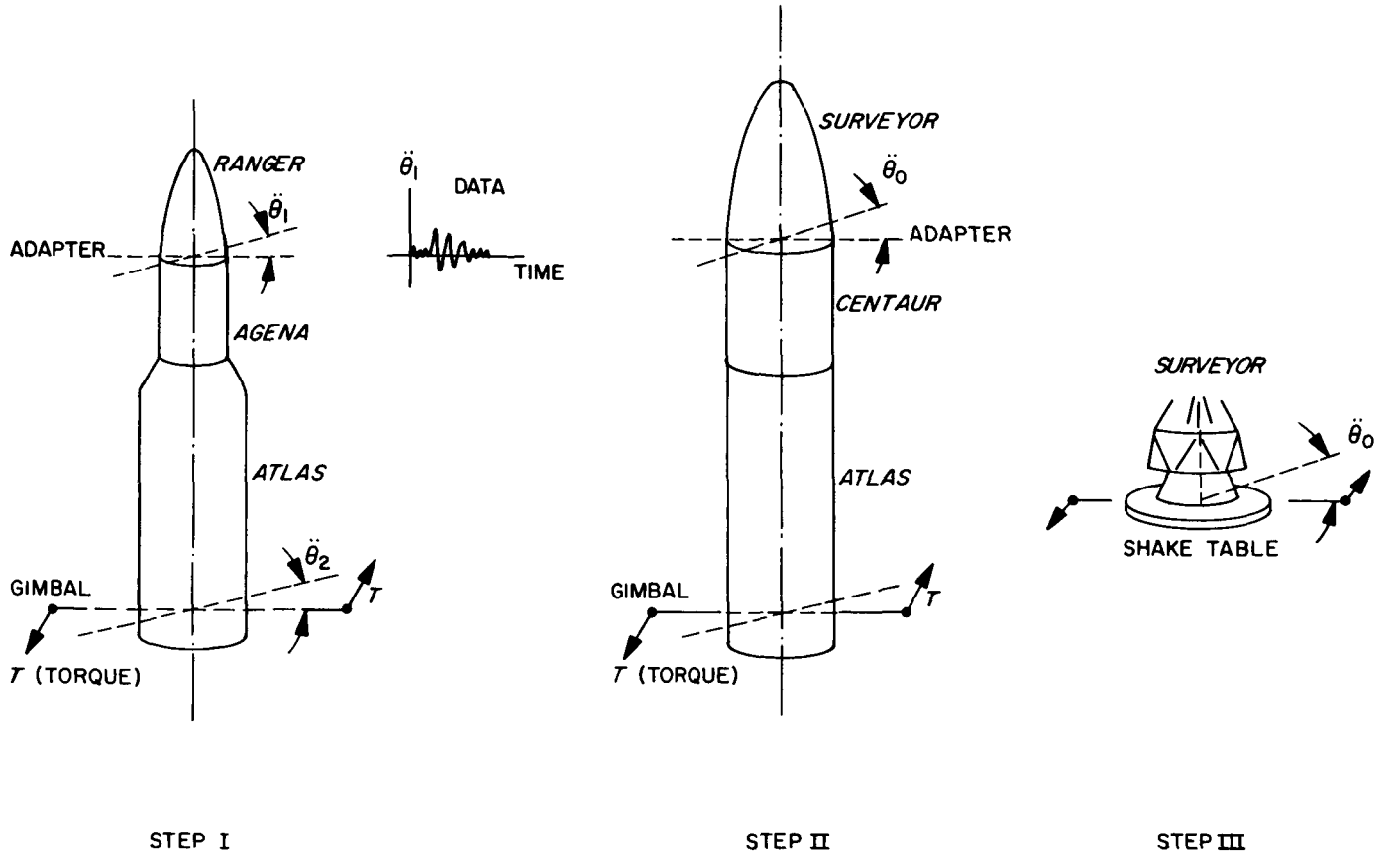

Fig. 1. Surveyor torsional load analysis and torsional test

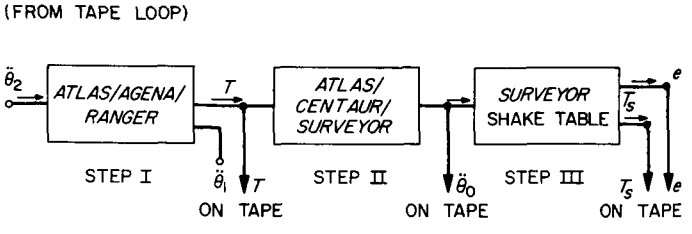

$\ddot{\theta}_2$ GIMBAL BLOCK ACCELERATION (SYNTHESIZED)
$\ddot{\theta}_1$ *RANGER* ADAPTER ACCELERATION
T GIMBAL BLOCK TORQUE
$\ddot{\theta}_0$ *SURVEYOR* ADAPTER ACCELERATION
T_S TORQUE TO BE APPLIED BY SHAKERS
e ARMATURE VOLTAGE

Fig. 2. Analog simulation

A. Step I

A dynamic mathematical model was constructed for the *Atlas/Agena/Ranger* (Ref. 2), and a modal combination digital program provided the corresponding set of normal modes. Eight of these modes were retained to represent the structure in the frequency range from 12.6 to 147 cps and the accelerations at the adapter and gimbal block locations. The forced vibration of the structure in torsion can then be represented by a set of uncoupled nonhomogeneous differential equations obtained from the normal modes (Refs. 3 and 4), viz:

$$\ddot{q}_i + 2\xi_i\omega_i\dot{q}_i + \omega_i^2\dot{q}_i = \frac{\phi_{2i}}{m_i}T, \qquad i = 1,2,3,\cdots,N \tag{1}$$

where q_i are the generalized coordinates (normal); ω_i the natural frequencies; m_i the generalized masses (in torsion); ξ_i the reduced damping; and ϕ_{2i} are the modal displacements at the gimbal blocks. Since we are dealing here with a free-free vehicle in torsion, the rigid body mode (roll) must be considered. This mode is obtained from Eq. (1) by setting $\omega_i = 0$ and $\phi_{2i} = 1$. Calling $i = 0$ the rigid body mode, we have

$$\ddot{q}_0 = \frac{T}{m_0}, \tag{2}$$

where m_0 is the roll mass moment of inertia of the complete space vehicle. Let us note here that Eq. (2) is simply Newton's law for a rigid body rotation.

The angular acceleration $\ddot{\theta}_1$ at the *Ranger* adapter and $\ddot{\theta}_2$ at the gimbal blocks are obtained by a linear combination of all the modes including the rigid body mode.

$$\ddot{\theta}_1 = \sum_{i=0}^{N} \phi_{1i}\ddot{q}_i, \tag{3}$$

$$\ddot{\theta}_2 = \sum_{i=0}^{N} \phi_{2i}\ddot{q}_i, \tag{4}$$

where ϕ_{1i} are the modal displacements at the *Ranger* adapter.

Noting that, for the rigid body mode, we have $\phi_{10} = \phi_{20} = 1$, and substituting Eq. (2) into (3) and (4), we obtain:

$$\ddot{\theta}_1 = \frac{T}{m_0} + \sum_{i=1}^{N} \phi_{1i}\ddot{q}_i, \tag{5}$$

$$T = m_0\ddot{\theta}_2 - m_0 \sum_{i=1}^{N} \phi_{2i}\ddot{q}_i. \tag{6}$$

Written in terms of the *Atlas/Agena/Ranger* vehicle characteristics, we finally obtain the set of Eqs. (7) through (16) (Appendix B).

$$\ddot{q}_1 + 4.75\dot{q}_1 + 6250q_1 = -0.984 \quad 10^{-5}T \tag{7}$$

$$\ddot{q}_2 + 13.0\dot{q}_2 + 46{,}940q_2 = -1.23 \quad 10^{-5}T \tag{8}$$

$$\ddot{q}_3 + 20.8\dot{q}_3 + 120{,}700q_3 = -0.604 \quad 10^{-5}T \tag{9}$$

$$\ddot{q}_4 + 25.5\dot{q}_4 + 180{,}500q_4 = -1.39 \quad 10^{-5}T \tag{10}$$

$$\ddot{q}_5 + 30.1\dot{q}_5 + 251{,}500q_5 = -0.825 \quad 10^{-5}T \tag{11}$$

$$\ddot{q}_6 + 30.5\dot{q}_6 + 255{,}600q_6 = -1.38 \quad 10^{-5}T \tag{12}$$

$$\ddot{q}_7 + 41.6\dot{q}_7 + 483{,}100q_7 = -1.32 \quad 10^{-5}T \tag{13}$$

$$\ddot{q}_8 + 56.5\dot{q}_8 + 855{,}200q_8 = -0.855 \quad 10^{5}T \tag{14}$$

These equations were simulated on the analog computer. The time scale factor from real time to computer time was chosen at 32 to be compatible with the maximum tape-recorder speed ratio. Consequently, all input and output signals relative to the analog were recorded at 1⅞ in./sec; the recorder was played back at 60 in./sec to obtain the data in real time. The damping for these modes was assumed to be viscous at 3% critical for all modes. This value was found to be the most realistic when comparing pulse shapes obtained on the computer with the pulse shapes obtained in flight.

In the basic problem, the acceleration at the adapter $\ddot{\theta}_1$ is given and the torque T is the unknown output; this case corresponds to Eqs. (1) and (5). Unfortunately, this set of equations was found to be unstable on the analog as could be expected from inspection of the homogeneous solution, which has the form of a positive exponential time function. This instability is due to the different signs that the mode shapes ϕ_{1i} and ϕ_{2i} have for certain modes. Looking at the problem from a different viewpoint, it was recognized that the analog system would always be stable if the input were the acceleration $\ddot{\theta}_2$ at the gimbal blocks rather than the acceleration $\ddot{\theta}_1$ at the adapter; i.e., if Eqs. (1) and (6) were used rather than (1) and (5). The stability of this system, (1) and (6), is ensured by virtue of the same modal displacements ϕ_{2i} being used in both equations, since input and output are taken at the same location on the structure (i.e., the gimbal blocks).

However, as mentioned previously, the gimbal block acceleration data were not usable; therefore, a synthetic pulse signal was constructed to replace these gimbal block data $\ddot{\theta}_2$. The synthesis was made in such a way that the corresponding acceleration $\ddot{\theta}_1$ at the *Ranger* adapter would have the same shock spectrum (or at least as close as could be) as the one obtained from the flight acceleration at the same adapter. The damping coefficient for this shock spectrum computation was taken as zero. The shock spectrum criterion was used here rather than the more rational Fourier transform only for reasons of expediency and simplicity. It is quite clear that the nonunique relationship between the time history of the acceleration and the shock spectrum does impair the result;

$$T = 105{,}400\ddot{\theta}_2 + 10{,}380\ddot{q}_1 + 12{,}950\ddot{q}_2 + 6360\ddot{q}_3 + 14{,}660\ddot{q}_4 + 8700\ddot{q}_5 + 14{,}560\ddot{q}_6 + 13{,}900\ddot{q}_7 + 9010\ddot{q}_8 \tag{15}$$

$$\ddot{\theta}_1 = 0.950 \quad 10^{-5}T - 0.126\ddot{q}_1 + 1.41\ddot{q}_2 + 0.343\ddot{q}_3 - 0.578\ddot{q}_4 + 0.152\ddot{q}_5 - 0.467\ddot{q}_6 + 0.415\ddot{q}_7 + 0.163\ddot{q}_8 \tag{16}$$

however, this objection was minimized by a choice of physically realistic time functions.

Since the flight acceleration at the adapter was clearly of a transient nature and the shock spectrum exhibited a finite number of peaks, a pulse of the following form was presupposed for $\ddot{\theta}_2$ and constructed on the analog computer

$$\ddot{\theta}_2 = t \sum_{i=1}^{n} a_i e^{-\beta_i t} \sin 2\pi f_i t, \qquad (17)$$

where f_i corresponds to the frequency of each major peak of the *Ranger* adapter acceleration $\ddot{\theta}_1$ shock spectrum and a_i and β_i are determined by trial and error. To facilitate this trial and error construction, it is noted that the term a_i is directly related to the amplitude of the peak at f_i, and β_i is directly related to the width of the same peak. The numerical values of the coefficients of Eq. (17) are indicated in Appendix C.

Once the proper synthesis is made, $\ddot{\theta}_2$ is used as an input for the *Atlas/Agena/Ranger* analog setup, i.e., Eqs. (7) through (16); then the torque T and the acceleration $\ddot{\theta}_1$ at the adapter are obtained simultaneously. The three signals ($\ddot{\theta}_2$, T, and $\ddot{\theta}_1$) were recorded on magnetic tape. Figures 3 through 6 show the shock spectrum of the flight accelerations at the *Ranger* adapter $\ddot{\theta}_1$ together with the shock spectrum for the same accelerations obtained from the synthetic input $\ddot{\theta}_2$. It must be noted that the matching of shock spectra for frequencies higher than 100 cps was not attempted. The reason for this is two-fold: (1) The mathematical model of the *Atlas/Agena/Ranger*

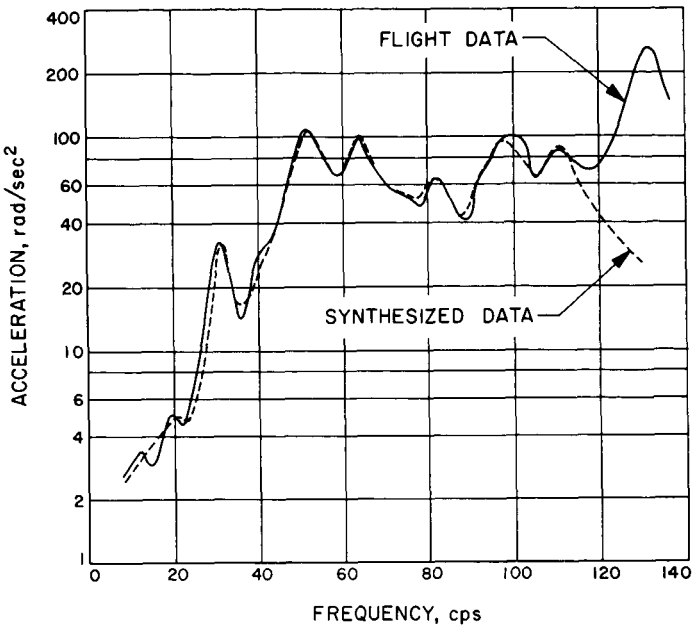

Fig. 4. Adapter acceleration shock spectra for *Ranger VII*

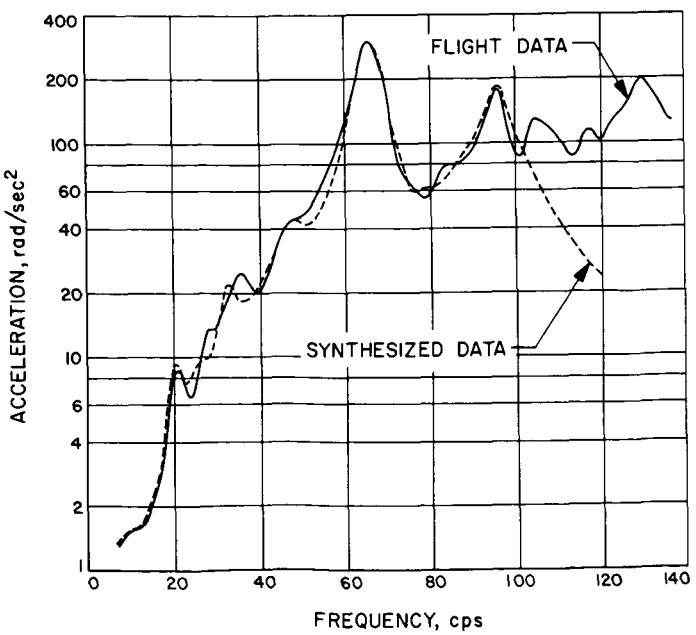

Fig. 3. Adapter acceleration shock spectra for *Ranger VI*

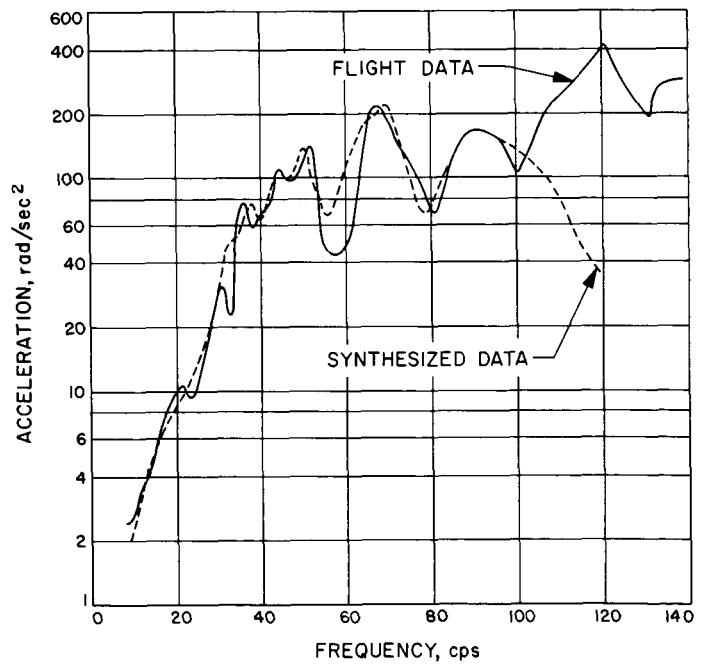

Fig. 5. Adapter acceleration shock spectra for *Ranger VIII*

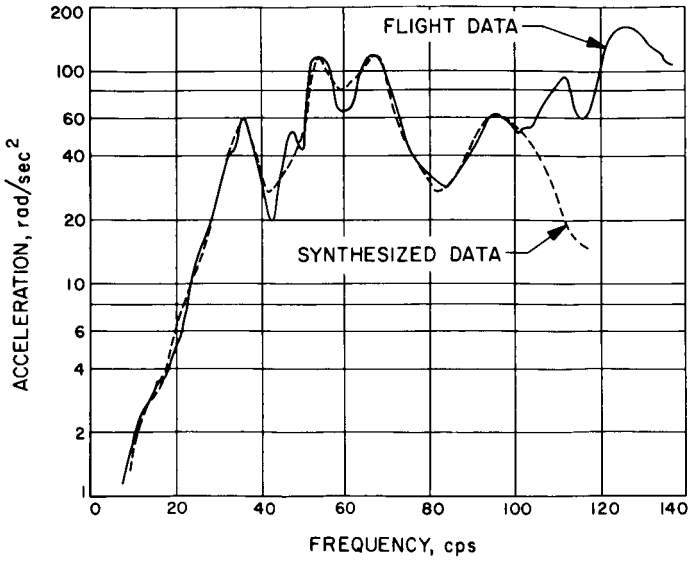

Fig. 6. Adapter acceleration shock spectra for *Ranger IX*

needed upgrading for the high-frequency range; (2) The high-frequency components of the signal are most likely to be strongly affected by electronic noise. Several attempts were made to match the high frequencies, but the torque required to reproduce those frequencies was found to be unrealistic.

B. Step II

In the second step, the *Atlas/Centaur/Surveyor* vehicle was analyzed. It was assumed that, since the thrust is a characteristic of the engine with no effect of the structure and since both vehicles (the *Atlas/Agena/Ranger* and the *Atlas/Centaur/Surveyor*) make use of the same booster, they were subjected to the same load at BECO event.

The analysis is similar to the one indicated in the first step. Equations of the type (1) and (5) also hold for the vibration of this structure; the only difference lies in the coefficients and in the selected number of modes. Rewritten here for convenience, these equations are

$$\ddot{q}_i + 2\xi_i\omega_i\dot{q}_i + \omega_i^2 q_i = \frac{\phi_{2i}}{m_i} T \tag{18}$$

$$\ddot{\theta}_0 = \frac{T}{m_0} + \sum_{i=1}^{N} \phi_{0i}\ddot{q}_i \tag{19}$$

where $\ddot{\theta}_0$ is the angular acceleration at the *Surveyor* adapter (field joint), ϕ_{0i} are the mode shapes at the adapter, and T is now a *given* function of time. Similarly to the first step, the numerical coefficients for Eqs. (18) and (19) were derived from a dynamic mathematical model (Ref. 2) representing the torsional characteristics of the *Atlas/Centaur/Surveyor* vehicle and from which the normal modes were obtained on a digital computer. There were 15 modes selected and a damping of 3% critical was chosen for all modes (Appendix B). Equations (20) through (35) represent these 15 modes and the acceleration at the *Surveyor* adapter.

$$\ddot{q}_1 + 4.4\dot{q}_1 + 5441q_1 = -0.237 \quad 10^{-5}T \tag{20}$$

$$\ddot{q}_2 + 4.7\dot{q}_2 + 5843q_2 = -0.219 \quad 10^{-5}T \tag{21}$$

$$\ddot{q}_3 + 5.4\dot{q}_3 + 7985q_3 = -0.759 \quad 10^{-5}T \tag{22}$$

$$\ddot{q}_4 + 6.3\dot{q}_4 + 11{,}140q_4 = -0.441 \quad 10^{-5}T \tag{23}$$

$$\ddot{q}_5 + 6.4\dot{q}_5 + 11{,}390q_5 = -1.930 \quad 10^{-5}T \tag{24}$$

$$\ddot{q}_6 + 17.1\dot{q}_6 + 81{,}490q_6 = -0.803 \quad 10^{-5}T \tag{25}$$

$$\ddot{q}_7 + 20.6\dot{q}_7 + 116{,}600q_7 = -0.226 \quad 10^{-5}T \tag{26}$$

$$\ddot{q}_8 + 25.5\dot{q}_8 + 179{,}900q_8 = -2.119 \quad 10^{-5}T \tag{27}$$

$$\ddot{q}_9 + 26.4\dot{q}_9 + 194{,}500q_9 = -0.205 \quad 10^{-5}T \tag{28}$$

$$\ddot{q}_{10} + 36.4\dot{q}_{10} + 368{,}400q_{10} = -0.595 \quad 10^{-5}T \tag{29}$$

$$\ddot{q}_{11} + 41.5\dot{q}_{11} + 477{,}700q_{11} = -0.797 \quad 10^{-5}T \tag{30}$$

$$\ddot{q}_{12} + 49.0\dot{q}_{12} + 667{,}200q_{12} = -0.733 \quad 10^{-5}T \tag{31}$$

$$\ddot{q}_{13} + 50.0\dot{q}_{13} + 694{,}600q_{13} = -0.761 \quad 10^{-5}T \tag{32}$$

$$\ddot{q}_{14} + 54.6\dot{q}_{14} + 830{,}200q_{14} = -0.264 \quad 10^{-5}T \tag{33}$$

$$\ddot{q}_{15} + 59.6\dot{q}_{15} + 986{,}800q_{15} = -0.946 \quad 10^{-5}T \tag{34}$$

$$\begin{aligned}\ddot{\theta}_0 = 0.540 \quad & 10^{-5}T + 0.108\ddot{q}_1 - 0.095\ddot{q}_2 + 0.038\ddot{q}_3 \\ & + 0.082\ddot{q}_4 + 0.358\ddot{q}_5 - 0.498\ddot{q}_6 - 0.164\ddot{q}_7 \\ & + 0.052\ddot{q}_8 + 1.347\ddot{q}_9 - 0.827\ddot{q}_{10} + 0.507\ddot{q}_{11} \\ & + 0.153\ddot{q}_{12} - 0.217\ddot{q}_{13} - 0.860\ddot{q}_{14} + 0.341\ddot{q}_{15}\end{aligned} \tag{35}$$

These equations were then programmed on the analog computer, and the system was driven with the torque T recorded in Step I. The output of the analog represents the sought prediction of the acceleration time history $\ddot{\theta}_0$ of the *Surveyor* adapter at BECO. This output was recorded on magnetic tape; Figs. 7 through 10 show the time histories for $\ddot{\theta}_1$, $\ddot{\theta}_2$, T, and $\ddot{\theta}_0$ obtained from the data of *Rangers VI* through *IX*.

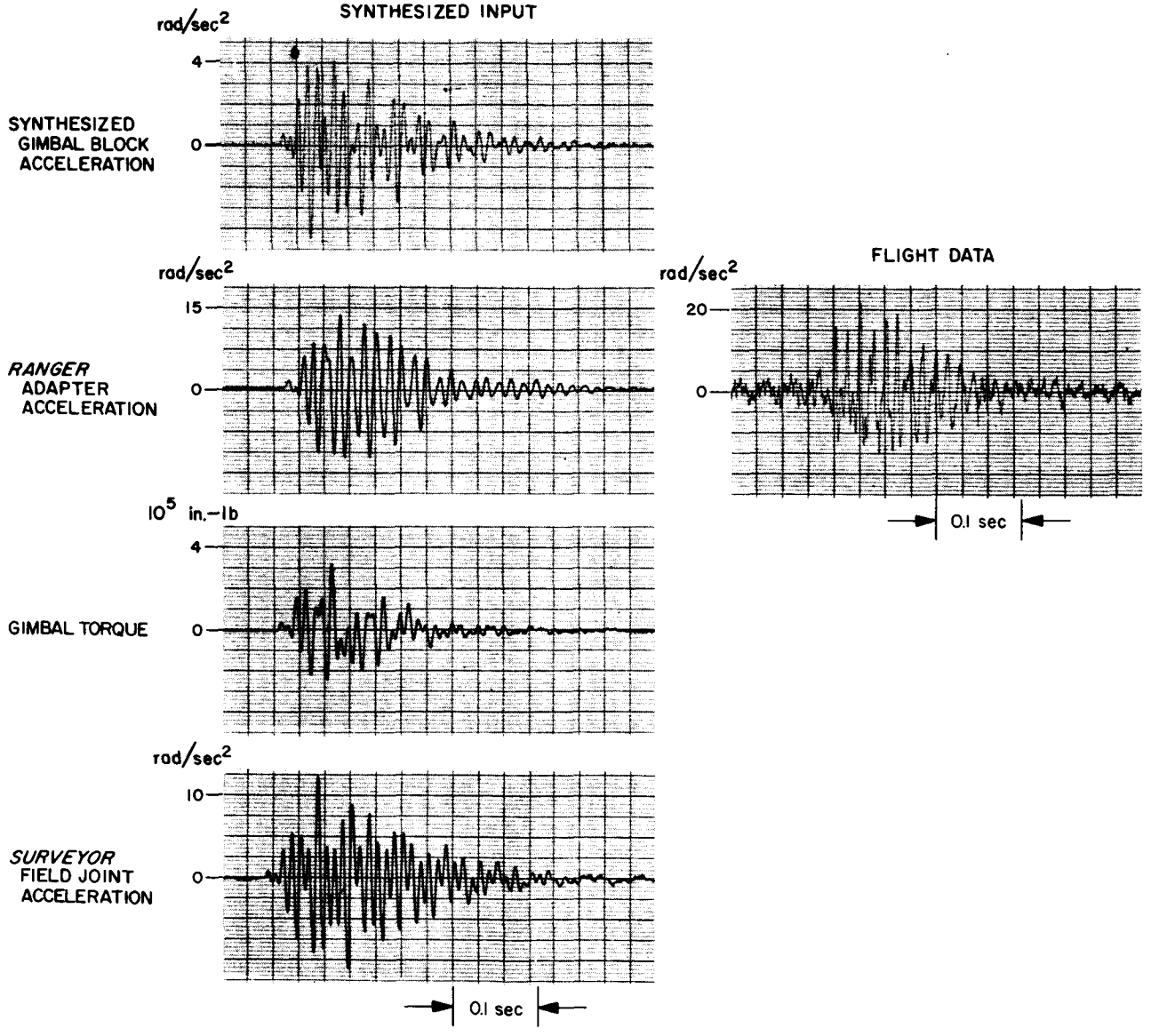

Fig. 7. Time histories for *Ranger VI*

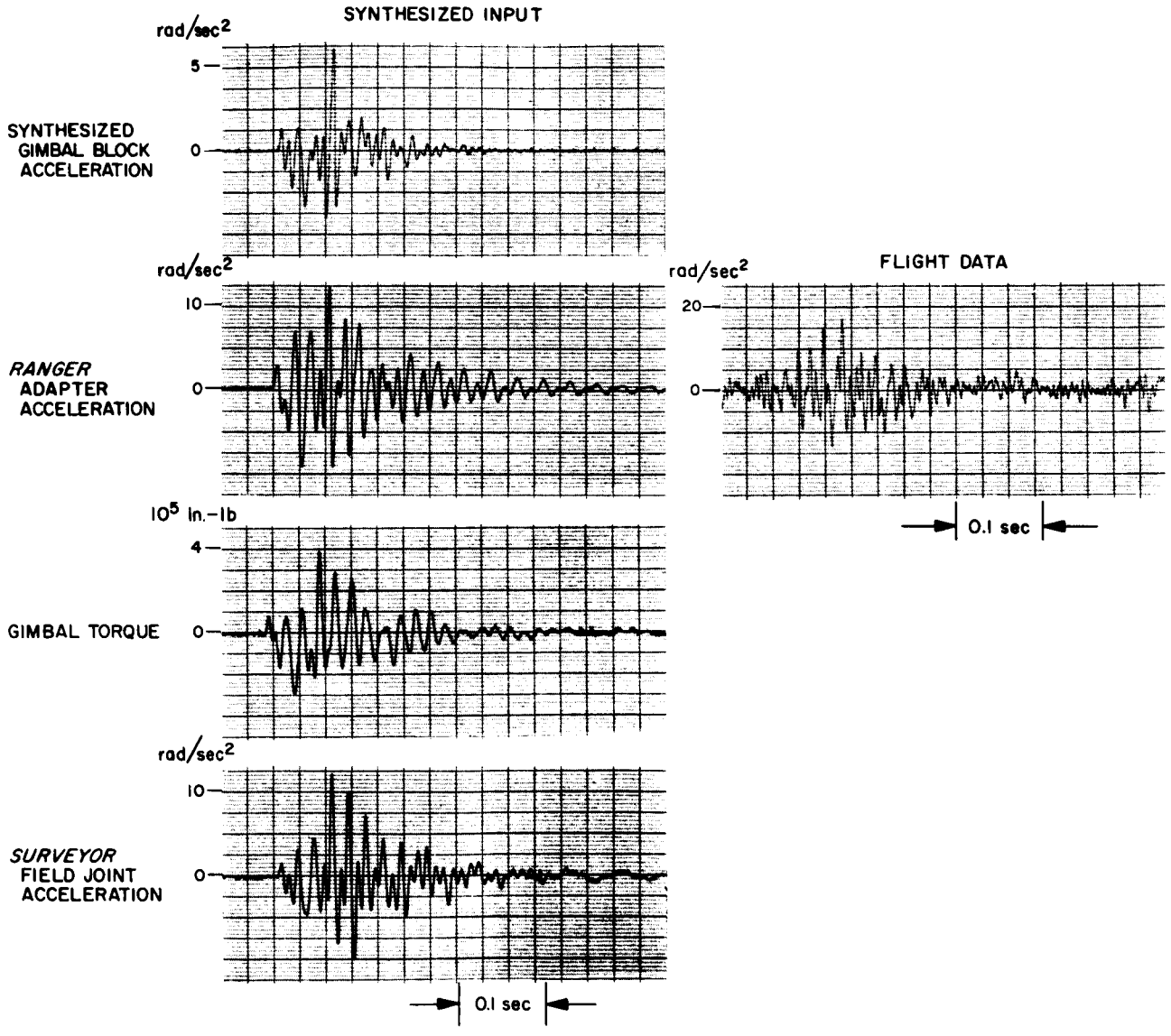

Fig. 8. Time histories for *Ranger VII*

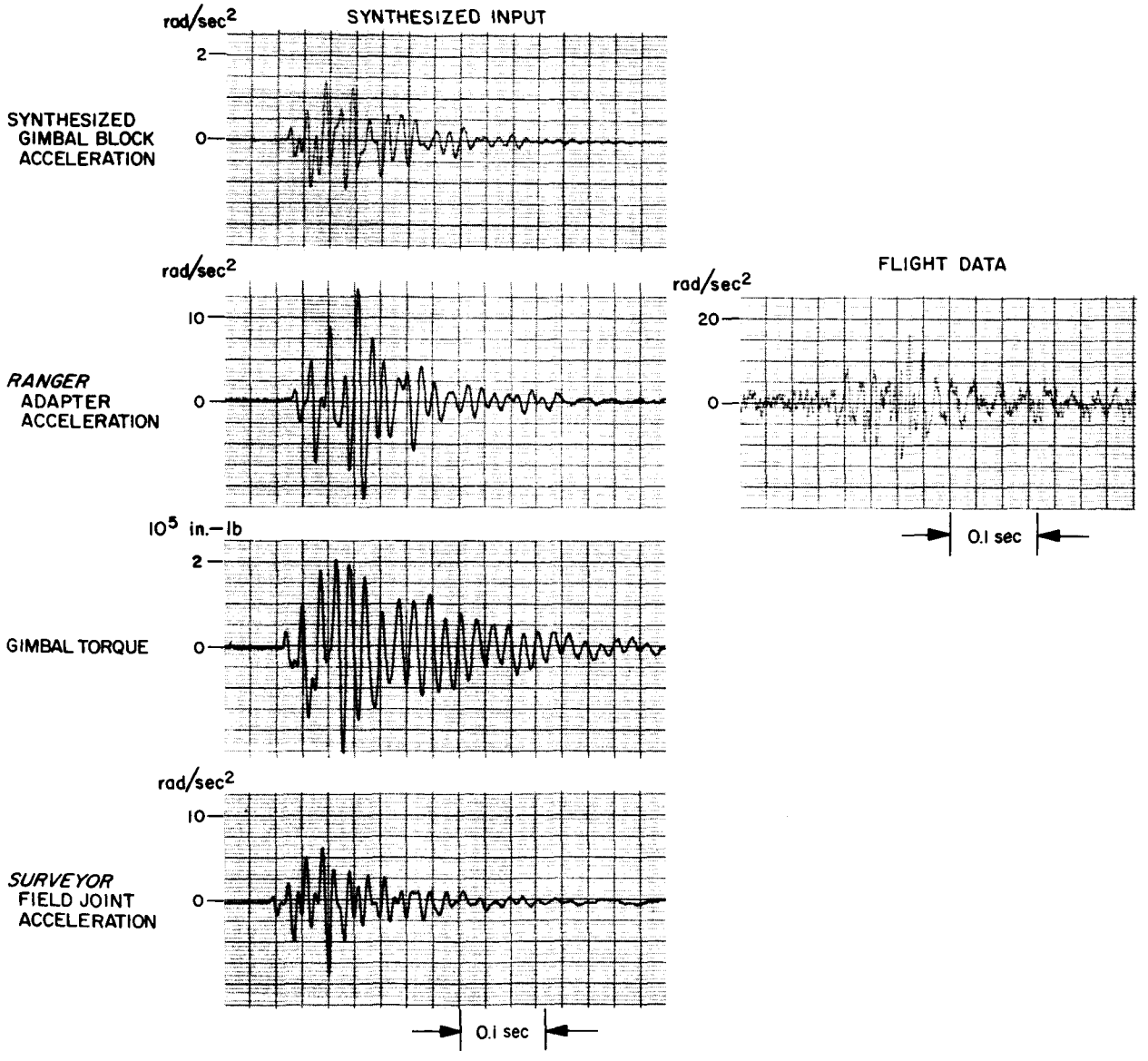

Fig. 10. Time histories for *Ranger IX*

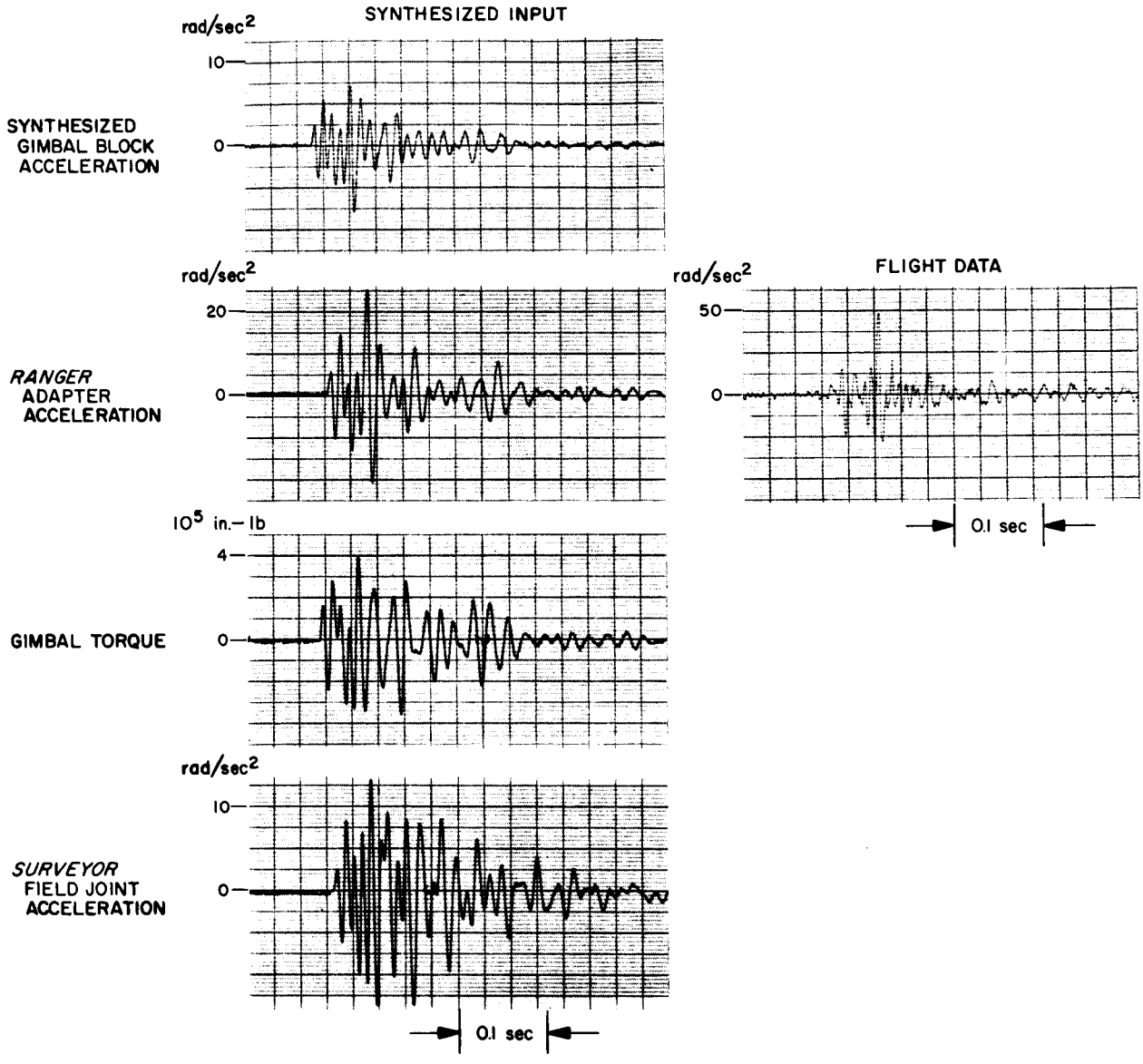

Fig. 9. Time histories for *Ranger VIII*

C. Step III

In this step, the attention was focused on the implementation of a test method to simulate the predicted environment on the actual spacecraft mounted on a shake table. Since the transient nature of the test imposed special constraints on the standard control system, a special analog equalization technique was developed. Here again, an analog computer solution was sought. An inverse simulation of the test was done on the analog computer in order to obtain the voltage to be applied at the armature of the shake table. To this end, the elastic characteristics of the spacecraft were introduced together with the electromechanical properties of the shakers and the fixture.

Three 1200-lb-shakers placed 120° apart were used for the test. The governing equations for the motion of the system are (Appendix C)

$$[M^{ee}]\{\ddot{q}\} + [C^{ee}]\{\dot{q}\} + [K^{ee}]\{q\} = -\{M^{er}\}\ddot{\theta}_0 \qquad (36)$$

$$T_s = \{M^{er}\}^T\{\ddot{q}\} + M^{rr}\ddot{\theta}_0 + K\theta_0 \qquad (37)$$

$$e = \frac{R}{\lambda l}T_s + \frac{L}{\lambda l}\dot{T}_s + 3\lambda l\dot{\theta}_0 \qquad (38)$$

where

$[M^{ee}] = \left[m_n^{ee}\right]$ = the diagonal generalized mass matrix of the spacecraft cantilevered at the base (field joint)

$[C^{ee}] = \left[c_n^{ee}\right]$ = the diagonal damping matrix

$[K^{ee}] = \left[k_n^{ee}\right]$ = the diagonal generalized stiffness matrix

$\{q\} = \{q_n\}$ = the column of the generalized displacement relative to the base

$\{M^{er}\} = \{m_n^{er}\}$ = the elastic mode rigid body rotation column.

M^{rr} = the total moment of inertia of the spacecraft and the shake table, including the fixture

$\ddot{\theta}_0$ = the given acceleration at the base

T_s = the torque developed by the shakers

e = the armature voltage

λ = the force/current coefficient

R = the resistance of each armature

L = the self-inductance of each armature

l = the distance from axis of rotation to the shakers

K = the elastic support in rotation

The matrices $[M^{ee}]$, $[C^{ee}]$, $[K^{ee}]$, and $\{M^{er}\}$ were originally obtained from a modal survey of the spacecraft (Ref. 5). However, this modal survey was made on a spacecraft somewhat different from the tested spacecraft. Consequently, $[M^{ee}]$, $[C^{ee}]$, $[K^{ee}]$, and $\{M^{er}\}$ were subsequently modified using the results of a low-level sine sweep made on the actual mounting at the rate of 1 octave/min. Figure 11 (solid curve) shows a plot of the armature voltage per unit angular acceleration in terms of the frequency obtained during this test. First, an evaluation of the coefficients of the matrices $[M^{ee}]$, $[C^{ee}]$, $[K^{ee}]$, and $\{M^{er}\}$ can be determined from this curve. To this end, it is noted that:

(1) The position of the peaks is directly related to the terms k_n^{ee}.

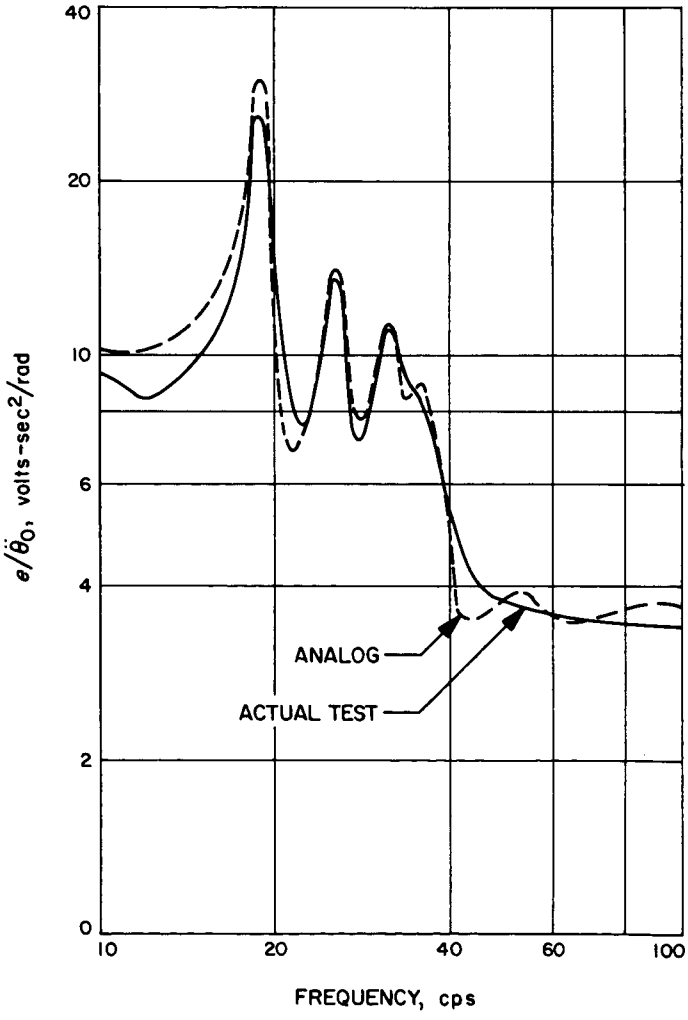

Fig. 11. Low-level sine sweep for Surveyor

(2) The height of the peaks is directly related to the terms m_n^{er}.

(3) The width of the peaks is directly related to the terms c_n^{ee}.

Then the corresponding equations [(36), (37), and (38)] were simulated on the analog computer and the relationship between the armature voltage and frequency measured as shown by the equalization curve (dashed curve) in Fig. 11. The coefficients were finally adjusted to match the two curves as closely as possible. The set of equations obtained from this matching is indicated below.

$$\ddot{q}_1 + 2.12\dot{q}_1 + 2818.5q_1 = 5.5\ddot{\theta}_0 \tag{39}$$

$$\ddot{q}_2 + 7.2\dot{q}_2 + 14{,}200q_2 = 27.7\ddot{\theta}_0 \tag{40}$$

$$\ddot{q}_3 + 12.9\dot{q}_3 + 25{,}600q_3 = 17.3\ddot{\theta}_0 \tag{41}$$

$$\ddot{q}_4 + 16.1\dot{q}_4 + 40{,}400q_4 = 15.0\ddot{\theta}_0 \tag{42}$$

$$\ddot{q}_5 + 23.0\dot{q}_5 + 51{,}000q_5 = 12.5\ddot{\theta}_0 \tag{43}$$

$$\ddot{q}_6 + 20.1\dot{q}_6 + 60{,}310q_6 = 10.9\ddot{\theta}_0 \tag{44}$$

$$\ddot{q}_7 + 26.0\dot{q}_7 + 105{,}930q_7 = 6.5\ddot{\theta}_0 \tag{45}$$

$$\ddot{q}_8 + 28.8\dot{q}_8 + 130{,}104q_8 = 0.58\ddot{\theta}_0 \tag{46}$$

$$\ddot{q}_9 + 30.0\dot{q}_9 + 142{,}121q_9 = 0.34\ddot{\theta}_0 \tag{47}$$

$$T_s = -5.5\ddot{q}_1 - 27.7\ddot{q}_2 - 17.3\ddot{q}_3 - 15.0\ddot{q}_4 - 12.5\ddot{q}_5 - 10.9\ddot{q}_6 - 6.5\ddot{q}_7 - 0.58\ddot{q}_8 - 0.34\ddot{q}_9 + 3575\ddot{\theta}_0 + 1.905 \quad 10^6\theta_0 \tag{48}$$

$$e = 2.361 \quad 10^{-3}T_s + 9.48 \quad 10^{-7}\dot{T}_s + 430.5\dot{\theta}_0 \tag{49}$$

It is noted here that the coefficients of Eqs. (46) and (47) correspond to the original modal survey and have not been modified by the sine sweep data, since the sine sweep curve did not show any significant peak above 50 cps. Those two equations have very little influence on the determination of the voltage e and the torque T_s (as can be seen from the low value of the coefficients m_n^{er}) and could have been dropped. However, they were retained because of their need in the equivalent sine sweep determination.

The tape containing $\ddot{\theta}_0$ was played back on the analog computer simulating Eqs. (39) through (49). The corresponding armature voltage e and the shaker torque T_s were then recorded on magnetic tape and are displayed in Figs. 12 through 15.

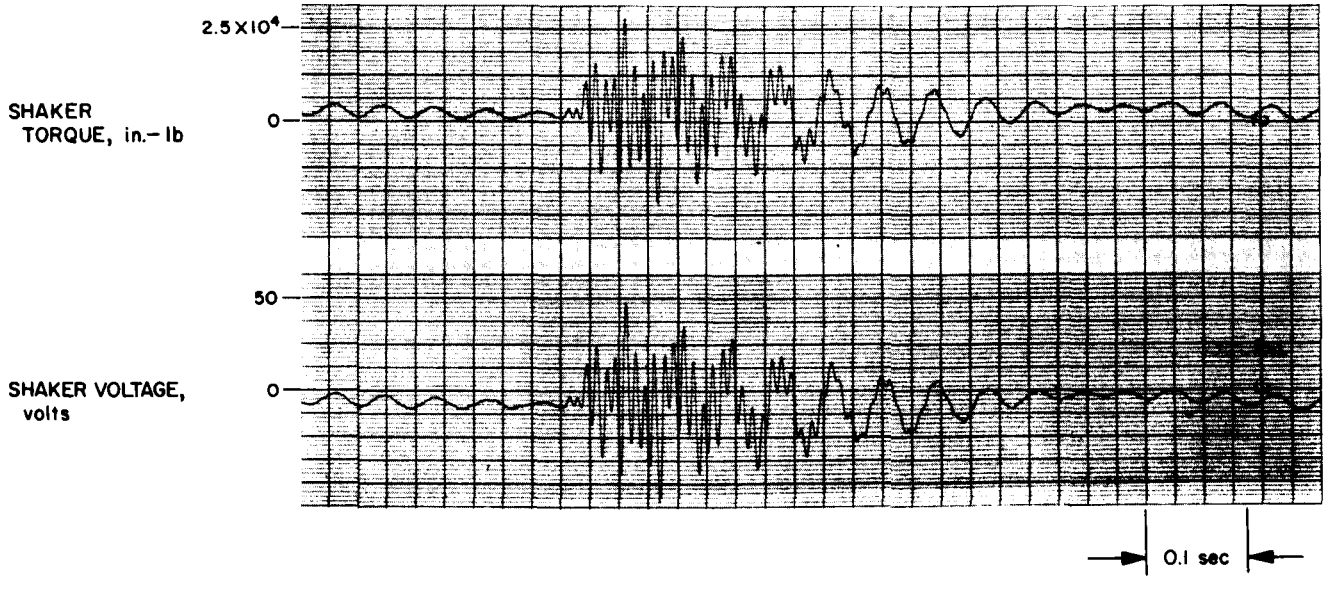

Fig. 12. Shaker time histories for *Ranger VI*

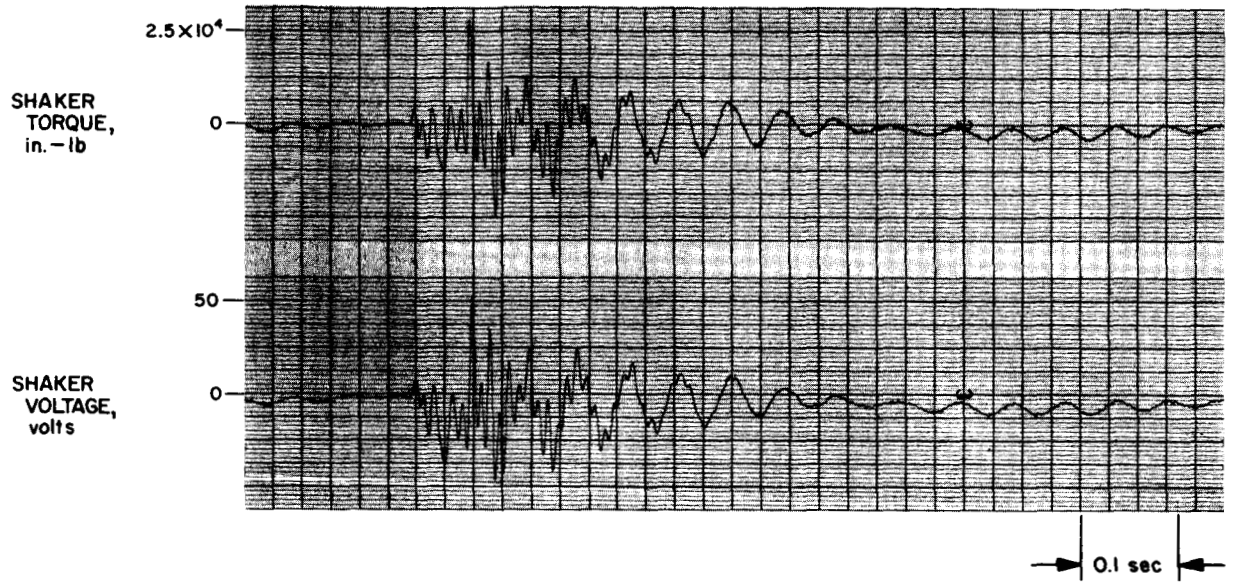

Fig. 13. Shaker time histories for *Ranger VII*

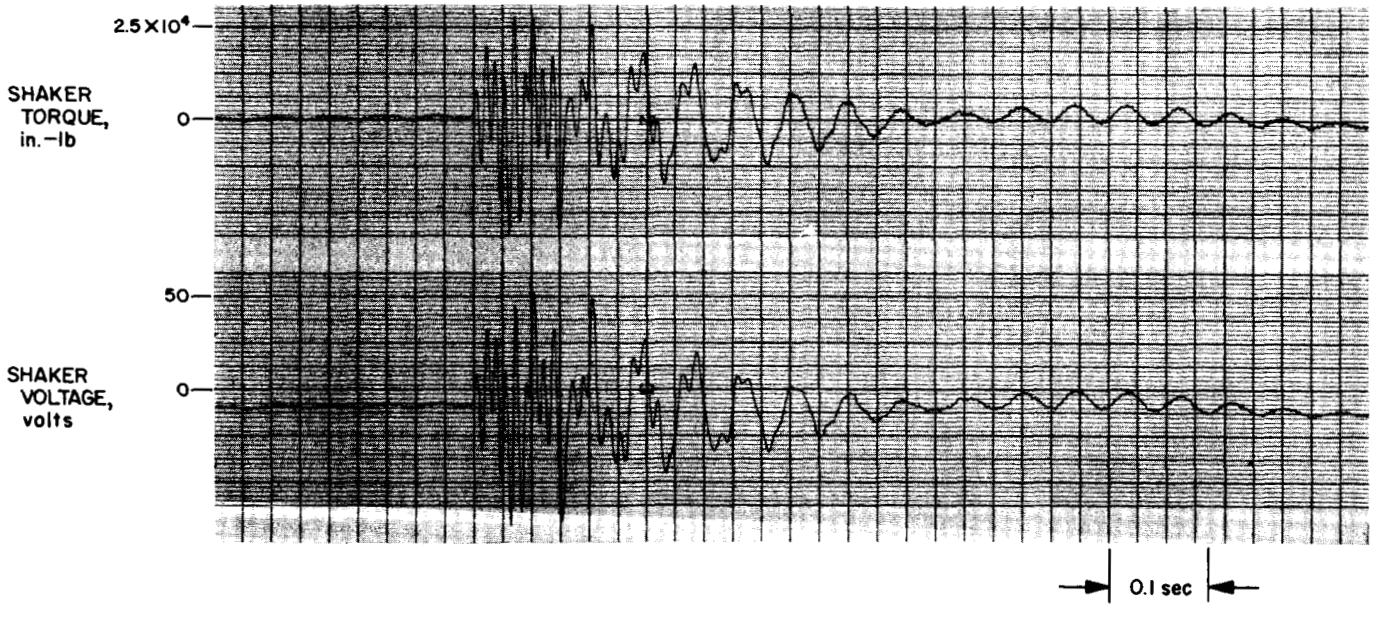

Fig. 14. Shaker time histories for *Ranger VIII*

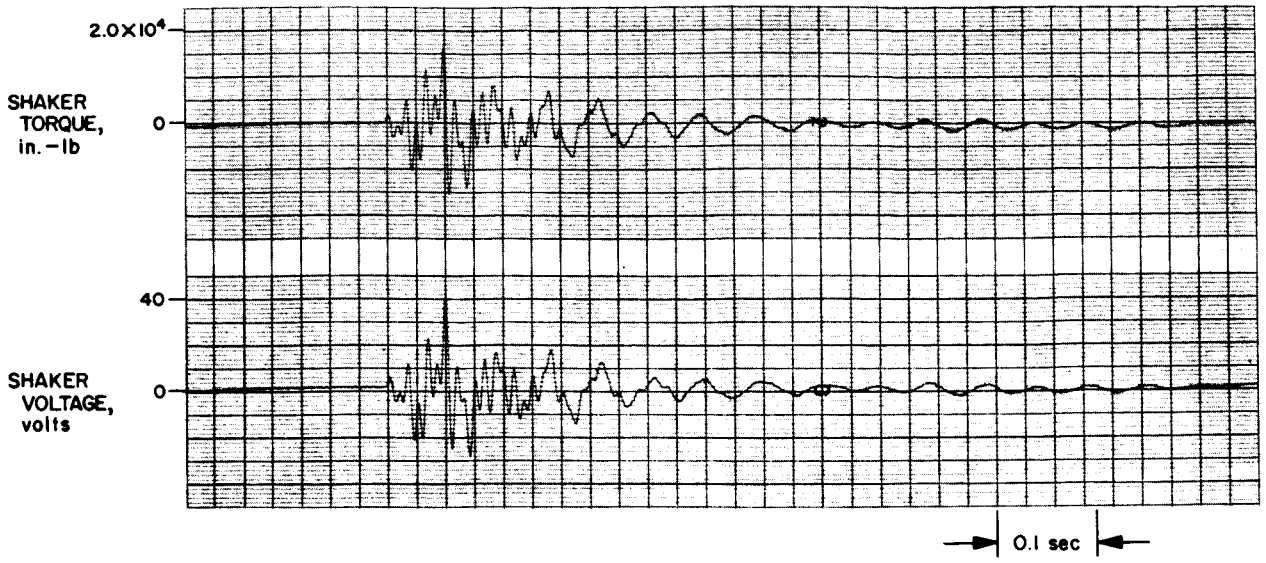

Fig .15. Shaker time histories for *Ranger IX*

IV. IMPLEMENTATION OF THE PULSE TESTING

All of the levels reported previously correspond to the flight prediction. However, to account for inaccuracies in the modal representations and in the *Ranger* flight data, the amplitude–time histories of the synthesized torque were arbitrarily doubled to inject an appropriate conservatism in the establishment of "limit loads" and the associated "limit accelerations" at the field joint of the *Surveyor* adapter. Then a factor of safety of 1.5 was used in defining ulimate conditions for the structural qualification tests. Therefore, the structural qualification test level was chosen to be three times the flight level. Figure 16 shows the four pulses representing the ultimate angular acceleration to be reproduced at the field joint of the *Surveyor* adapter. Those pulses have the same shape as the one indicated earlier; however, the scale is different in accordance with the required test level. Two different methods were used for the implementation of the test:

(1) *Method 1.* Since the equalization was included in the construction of the tape on the analog [Fig. 17(a)], the voltage tape e was played back through the power amplifier without the use of any equalization circuit.

(2) *Method 2.* The standard peak and notch equalizer was used, and the acceleration tape $\ddot{\theta}_n$ was fed into the equalizer in series with the power amplifier [Fig. 17(b)].

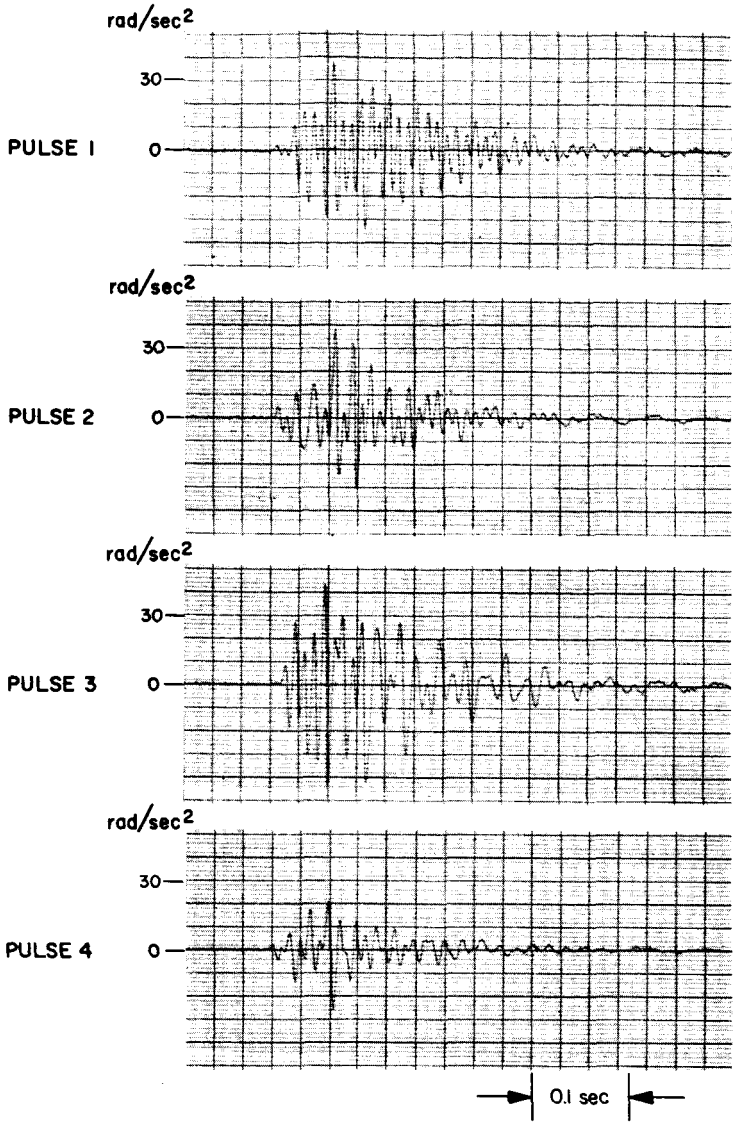

Fig. 16. Torsional pulse requirement, field joint acceleration

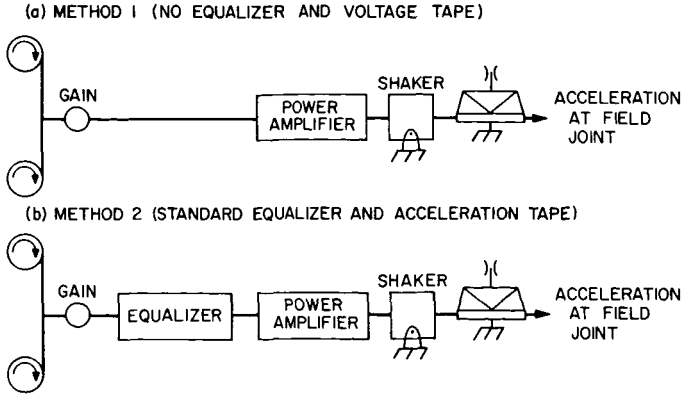

Fig. 17. Pulse testing implementation

V. RESULTS OF THE PULSE TESTING

The records of the acceleration, observed at the base of the spacecraft for each pulse during the test, are shown in Figs. 18 and 19. The shock spectra of these accelerations, together with the shock spectra of the desired accelerations, are shown in Figs. 20 through 23.

Method 1 gives the best agreement between the desired shock and the observed shock spectrum for pulses 1, 2, and 3. Although the structure was also tested for pulse 4, the record of the test was unusable. Instead, a slightly higher level pulse from another test is indicated on Fig. 23 to show that the shape of the spectrum is in agreement with the spectrum of the desired pulse. Method 2 also gives good results, although the shape of the observed spectra does not match the desired spectra with the same accuracy as for Method 1, especially in the critical region around 19 cps for which the level is two to three times lower. This relatively good fit of Method 2 shows that the phase shifts introduced by the peak and notch filters in the equalization process are not

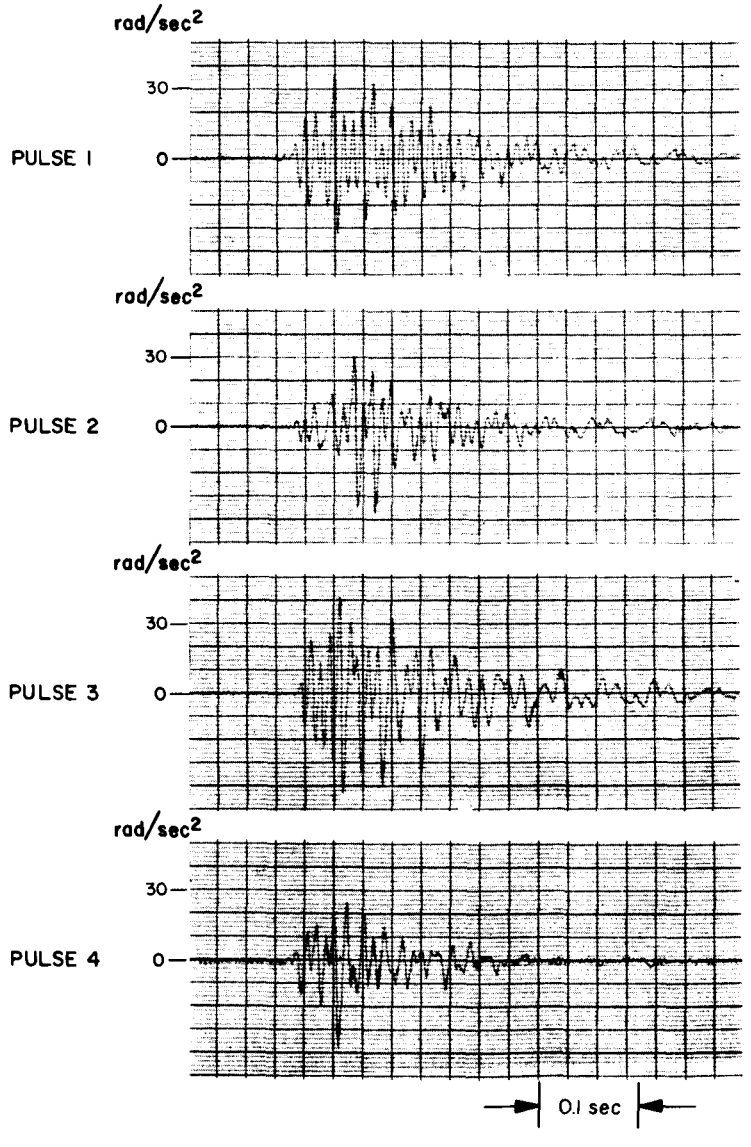

Fig. 18. Observed field joint acceleration, Method 1

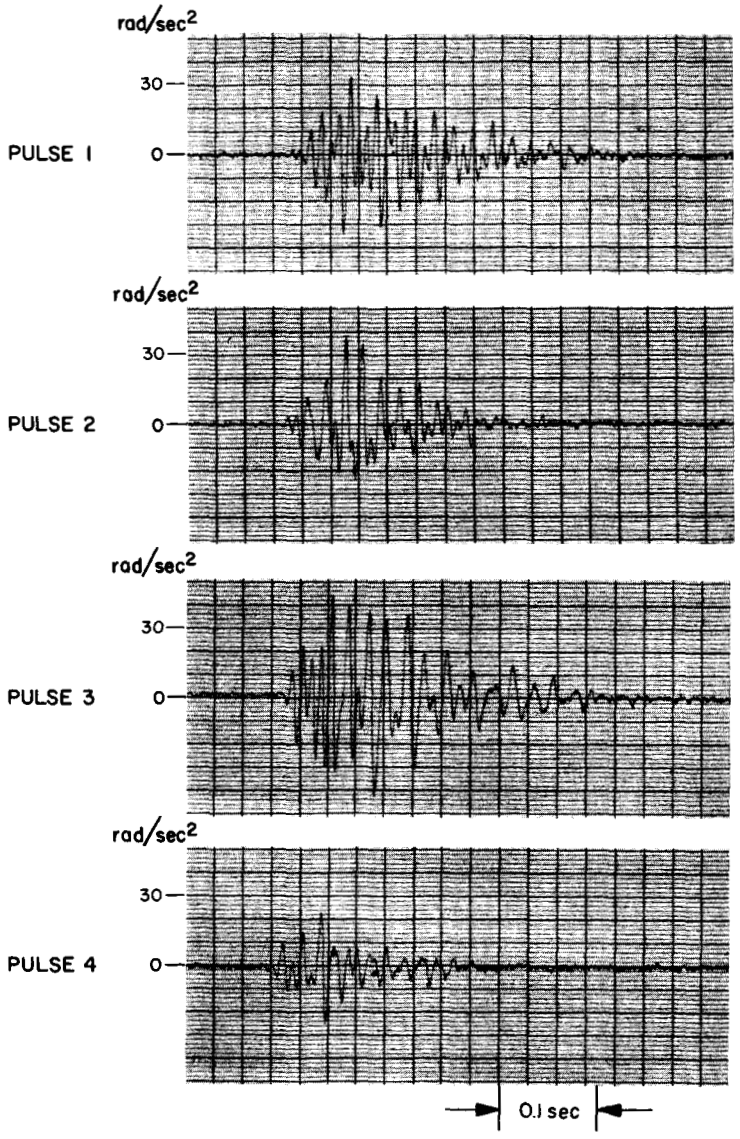

Fig. 19. Observed field joint acceleration, Method 2

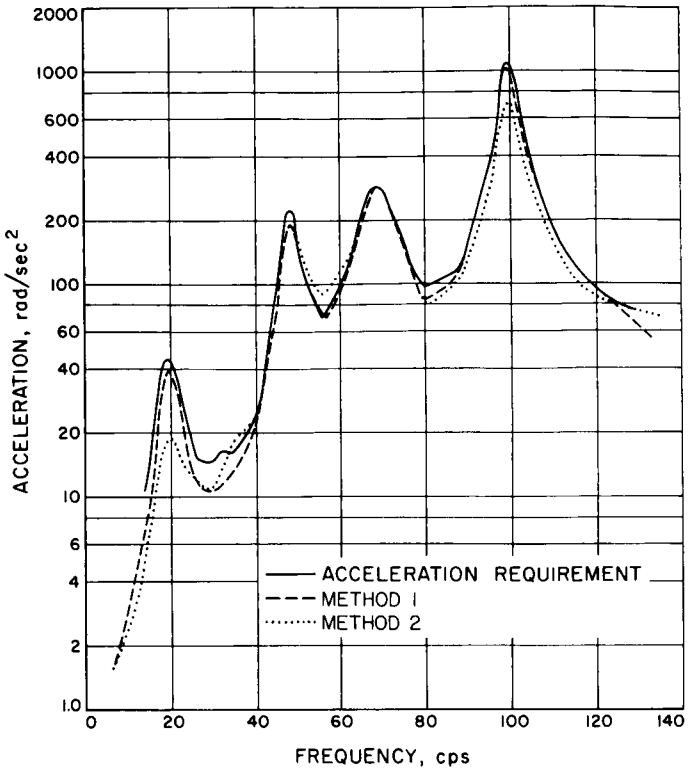

Fig. 20. Field joint acceleration shock spectrum, pulse 1

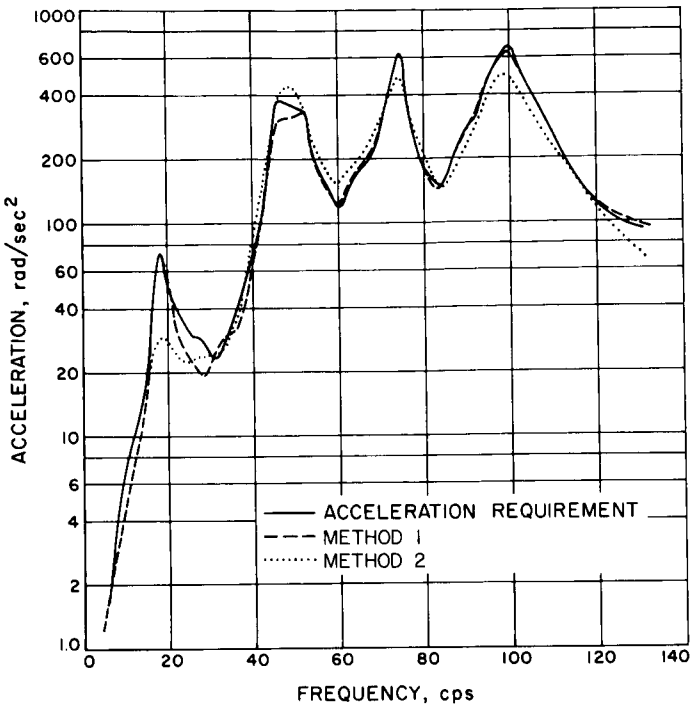

Fig. 22. Field joint acceleration shock spectrum, pulse 3

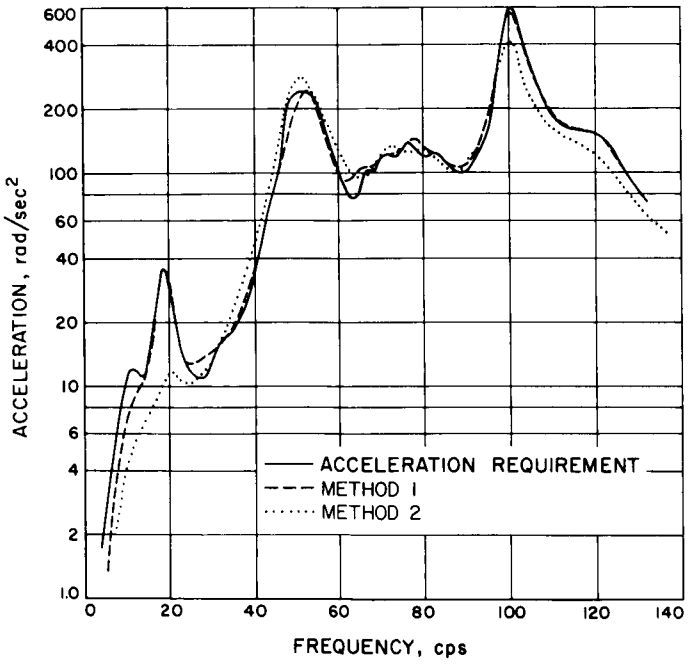

Fig. 21. Field joint acceleration shock spectrum, pulse 2

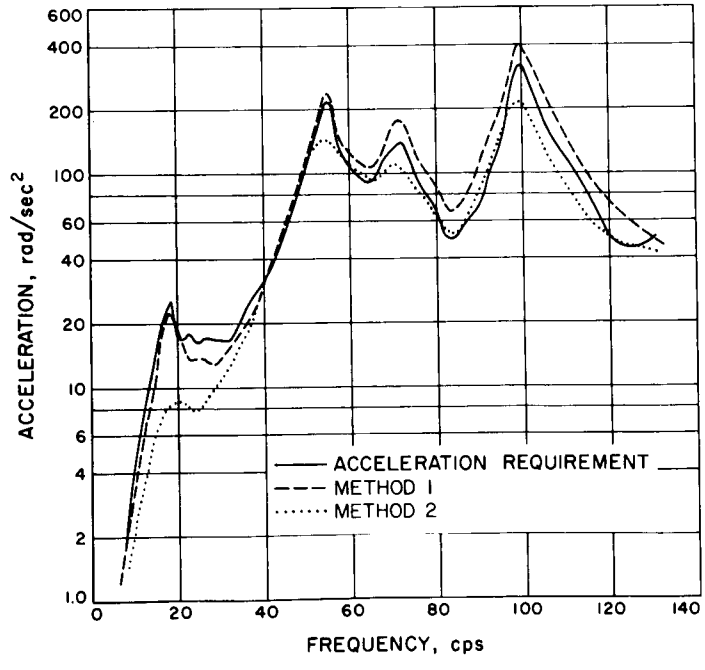

Fig. 23. Field joint acceleration shock spectrum, pulse 4

critical as far as the shock spectrum is concerned. In fact, this is to be expected, since the shock spectrum does not take into account the relative phase of the frequency components of a pulse.

Considering the level of the desired shock spectra (Figs. 20 through 23), it is essential for this test to focus one's attention to the low-level region below 30 cps rather than the high-level region above 30 cps because the most violent mode of excitation of the spacecraft occurs at 19 cps. The spacecraft responds almost exclusively to this low-level region, as can be seen in Fig. 24, which represents the shock spectrum of the response of compartment A to pulse 3, Method 1. This shock spectrum exhibits a peak at 19 cps, with little response above this value, although the shock spectrum of the base acceleration $\ddot{\theta}_0$ has a peak at 100 cps, which is ten times the level noted at 19 cps. To be more general, this remark shows that the highest peak of the base acceleration shock spectrum does not necessarily impart the most critical load on the spacecraft and that the seemingly negligible low-frequency part of the shock cannot be discarded, but must be faithfully reproduced in the pulse testing. Consequently, Method 1, which reproduces accurately the level around 19 cps, gives a much better testing condition than Method 2, which is markedly deficient in the low-frequency region as noted previously.

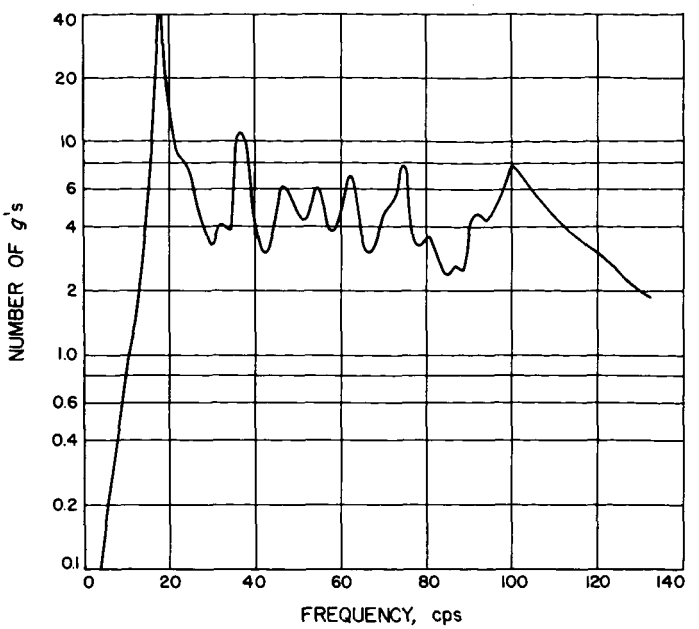

Fig. 24. Compartment A acceleration shock spectrum, pulse 3

VI. EQUIVALENT SINE SWEEP

Besides deriving the pulses used for the transient testing, the method described also gives extremely valuable data which can be used to formulate a sine sweep specification. Such a specification, supplementing the pulse-test definitions, can be justified pragmatically to account not only for errors in modal frequency prediction, but also for variations in modal frequencies among the space vehicles in the *Surveyor* Project.

In the sine sweep test, a sinusoidal acceleration,

$$\ddot{\theta} = A \sin \omega t, \tag{50}$$

at a slowly increasing frequency ω is imposed at the base of the spacecraft. Choosing the proper level for the amplitude A is always a difficult and controversial matter. Here this level was determined from the modal response $\ddot{q}_n$ $(n = 1, 2, 3, \cdots, 9)$ obtained during the simulation of the pulse test on the analog, which corresponds to Eqs. (39) through (47). The pulse $\ddot{\theta}_0$ was applied to the analog, and the time history of $\ddot{q}_1, \ddot{q}_2, \cdots, \ddot{q}_9$ was recorded. Figure 25 shows a typical record obtained during the simulation. From these records, the maximum $(\ddot{q}_n)_{max}$ of each $\ddot{q}_n$ was measured. Then the procedure was to replace the pulse $\ddot{\theta}_0$ by the equivalent sine wave,

$$\ddot{\theta}_n = A_n \sin \omega_n t \tag{51}$$

at the natural frequencies ω_n of each mode. The unknown amplitude A_n of this sine wave was determined in such a way that the amplitude of the sinusoidal modal response $\ddot{q}_n$ of the spacecraft at resonance in the sine test is equal to the maximum pulse response for the same mode. To this end, the driving force (51) is substituted into Eq. (36)

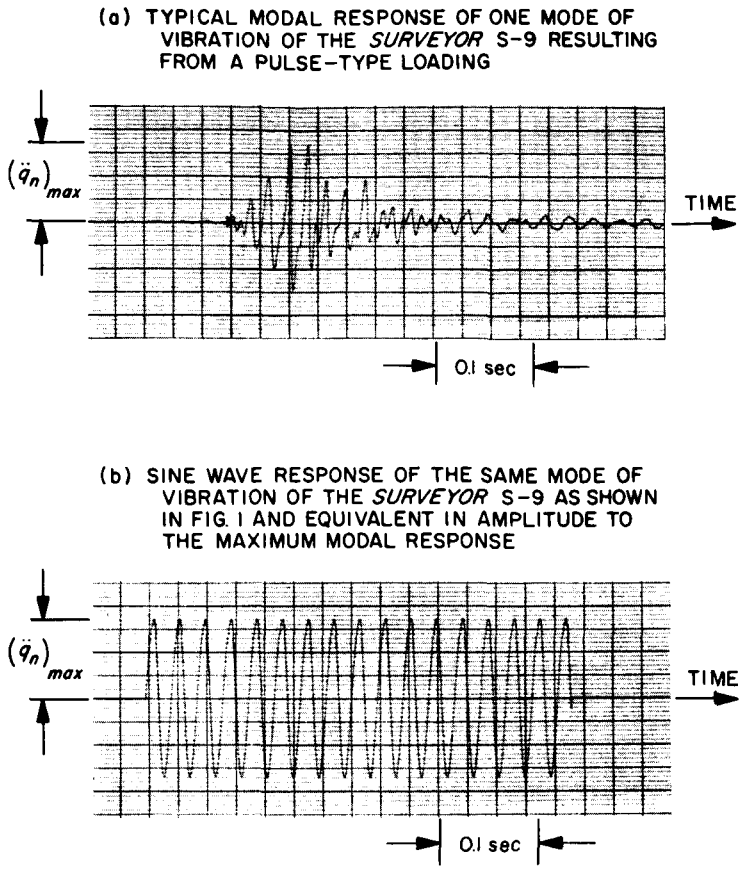

Fig. 25. Sine wave sweep equivalence

rewritten for each natural frequency ω_n. Noting that at resonance the inertia force is balanced by the spring force, we have:

$$2\xi_n\omega_n m_n^{ee}\dot{q}_n = -m_n^{er}A_n \sin\omega_n t, \qquad n = 1, 2, 3, \cdots, 9 \tag{52}$$

where ξ_n is the damping ratio for each mode. The corresponding acceleration $\ddot{q}_n$ is obtained by differentiation of Eq. (52).

$$\ddot{q}_n = -\frac{m_n^{er}}{2\xi_n m_n^{ee}} A_n \cos\omega_n t, \tag{53}$$

Finally, the amplitude of Eq. (53) is equated to the maximum pulse response $(\ddot{q}_n)_{max}$ to give

$$A_n = 2\xi_n \frac{m_n^{ee}}{|m_n^{er}|}(\ddot{q}_n)_{max}, \qquad n = 1, 2, \cdots, 9 \tag{54}$$

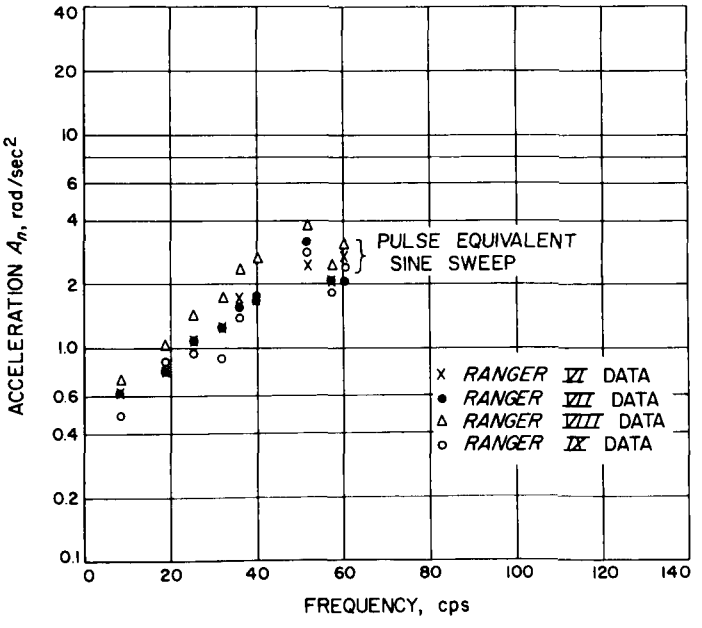

Fig. 26. *Surveyor* sine sweep recommendation

method is entirely dependent upon the availability of flight data and upon a mathematical model which is sufficiently representative of the structures involved. Both the quality of the data and its proper interpretation are, of course, of paramount importance. In this respect, the author stresses here that the mathematical model must have a high degree of sophistication in the neighborhood of the data transducers; otherwise local resonances will not be accounted for, thus resulting in a sizable and unacceptable degradation of the quality of the data. However, the model for the rest of the structure need not have the same degree of sophistication.

The location of the transducers is also a very important matter. Unfortunately, it is usually impossible to know in advance, with enough certainty, which locations would be the most appropriate, and the structural dynamicist should have the opportunity to revise the transducer locations late in the flight program, if needed, when more knowledge of the structure has been gained.

Finally, it is well known that most of the flight disturbances are transient in nature; therefore, pulse testing is far more realistic than the sine wave sweep testing. An equivalent sine sweep developed from the pulse data has been proposed here; however, although this equivalence has some rational basis, it is only an expedient which cannot, in any way, truly simulate the pulse testing.

The method has been successfully proved here for the *Surveyor* spacecraft, but is by no means restricted to that particular hardware. The ideas expressed in this report are rather general and should be beneficial for the evaluation of the dynamical behavior of other spacecraft structures as well.

In closing, mention is made that additional work is currently underway using the Fourier transform approach; this will put the analysis on a better footing and produce a method more flexible in its application.

APPENDIX A

Determination of the Input Data

Two accelerometers (Nos. 1 and 2) were diametrically located inside the *Agena/Ranger* adapter to record the accelerations in flight (Fig. A-1). The accelerometers were mounted to give linear tangential accelerations a_1 and a_2 both positive in the same tangential direction. The combination of the accelerations a_1 and a_2 was done at playback of the tape on an analog computer to obtain the angular acceleration $\ddot{\theta}_1$, according to

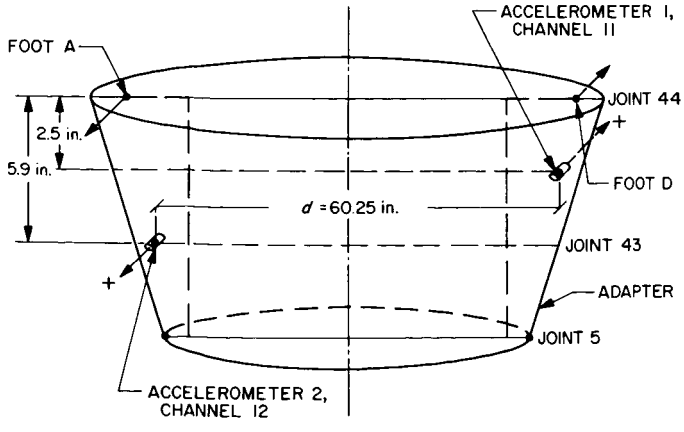

Fig. A-1. Accelerometer location

$$\ddot{\theta}_1 = \frac{\alpha_1 a_1 + \alpha_2 a_2}{d}, \qquad \text{(A-1)}$$

where d is the distance between the two accelerometers and α_1 and α_2 are weighting coefficients. The coefficients α_1 and α_2 were introduced to account for the geometric and elastic dissymmetry of locations 1 and 2. For a completely symmetric situation and a perfectly rigid adapter, we would have $\alpha_1 = \alpha_2 = 1$. The coefficients α_1 and α_2 were evaluated from a sinusodial excitation made at the first torsional natural frequency, $f = 66.4$ cps, of the spacecraft cantilevered on the adapter at joint 5 (Ref. 2).

Table 1. Equivalent sine sweep characteristics

f_n, cps	*Ranger VI* data		*Ranger VII* data		*Ranger VIII* data		*Ranger IX* data	
	$(\ddot{q}_n)_{max}$	A_n, rad/sec^2	$(\ddot{q}_n)_{max}$	A_n, rad/sec^2	$(\ddot{q}_n)_{max}$	A_n, rad/sec^2	$(\ddot{q}_n)_{max}$	A_n, rad/sec^2
8.45	83.5	0.61	83.5	0.61	100	0.73	66	0.48
19.0	361	0.78	361	0.78	486	1.05	398	0.86
25.5	232	1.08	232	1.08	318	1.48	202	0.94
32.0	234	1.25	234	1.25	334	1.78	166	0.89
36.0	215	1.73	208	1.67	304	2.43	176	1.46
40.0	230	1.69	238	1.74	368	2.70	229	1.68
51.8	200	2.45	262	3.22	308	3.80	230	2.82
57.4	15.0	2.09	15.0	2.09	18.0	2.48	14.0	1.93
60.0	12.5	2.94	9.0	2.10	13.0	3.06	10.5	2.47

Table 1 shows the different values of $(\ddot{q}_n)_{max}$ for each pulse of *Rangers VI* through *IX* and the corresponding equivalent sine sweep level A_n. Figure 26 shows a plot of A_n versus natural frequencies. An envelope of the data points can be used to determine the level of the sine sweep specification. Note that the data points at 57 and 60 cps correspond to the uncorrected equations, (46) and (47), and consequently do not have the same accuracy as the rest of the points on Fig. 26.

It must be noted here that the equivalent sine sweep, as shown, gives a test requirement which is on the conservative side, since during the sine sweep test the structure will respond in the vicinity of each natural frequency with a level close to $(\ddot{q}_n)_{max}$ for several cycles, while in the actual flight (and pulse test), it will reach the level $(\ddot{q}_n)_{max}$ only once. The number of cycles of the sine excitation clearly depends upon the sweep rate; intuitively, this conservatism will be somewhat relaxed by choosing a high sweep rate as opposed to a quasi-steady sine wave as is usually done.

Finally, it is important to note that the equivalence treated previously is a crude means of testing, primarily intended to make use of the existing sine sweep facilities for simulation of pulse testing. Also, it must be realized that no steady (or quasi-steady) sine wave excitation can produce the same effect as a pulse. One of the basic reasons is that a pulse excites a number of modes simultaneously, while the slow sine wave sweep gives dominant excitation in only one mode at a time. Here again, it can be expected that a sufficiently high sweep rate for the sine wave excitation would widen the range of frequencies through the buildup effect and make the test more realistic, although not quite equivalent to the pulse testing.

VII. CONCLUSIONS

A rational approach for the prediction of the flight acceleration of a spacecraft and the corresponding implementation of the vibration test requirement has been introduced here. Briefly, the method is an interplay between the flight data and the structures to yield rational means for writing and implementing the vibration specifications. It is not pretended that the method tested here for the *Surveyor* spacecraft is quite universal, but it represents, as far as the writer knows, a unique attempt to advance the state-of-the-art in deriving a vibration specification and in implementing the qualification test program. It is essential to say that the success of the

During this test, it was found that the reading of accelerometer 1 was 1.26 times the reading of accelerometer 2, clearly showing the dissymmetry indicated previously. The modal excitation also showed that the accelerations at the adjacent spacecraft feet (A and D) were nominally four times the accelerations 1 and 2. This was attributed to the flexibility of the adapter and the mounting brackets. Therefore, to account for this local flexibility, a new joint (No. 43, Fig. A-1) was introduced at the level of accelerometer 2 in the mathematical model of the *Agena* vehicle (Ref. 2). Accordingly, joint 43 became the data pickup station and the reading of accelerometer 1, which is above joint 43, had to be corrected. The correction was made according to the relative readings of accelerometers 1 and 2, assuming that if accelerometer 1 had been placed geometrically and elastically symmetric with respect to accelerometer 2, it would have read the same amplitude during the modal test. Consequently, the coefficients α_1 and α_2 are

$$\alpha_1 = \frac{1}{1.26} = 0.795, \tag{A-2}$$

$$\alpha_2 = 1.0. \tag{A-3}$$

After substituting into Eq. (A-1) and noting that $d = 60.25$ in., we obtain:

$$\ddot{\theta}_1 = 5.1a_1 + 6.4a_2. \tag{A-4}$$

APPENDIX B

Modal Representation of the Structures

A. *Atlas/Agena/Ranger*

The dynamic model representing the torsional characteristics of the *Atlas/Agena/Ranger* vehicle is a 47-degree-of-freedom spring mass system. The details of this model are indicated in Ref. 2. It is simply mentioned here that special attention was placed on the proper modeling of the *Atlas* engine and the *Agena* adapter. The first 11 normal modes corresponding to this model are indicated in Table B-1.

The two modes at 12.02 cps and 53.90 cps were not retained for the problem, since the product $\phi_{1i}\,\phi_{2i}$, which commands the response of any particular mode, was much smaller for those two modes than for the other

Table B-1. Normal modes for *Atlas/Agena/Ranger*

f_i, cps	ω_i, rad/sec	Joint 43 Adapter accelerometers	Joint 41 Gimbal blocks	$\phi_{1i}\ \phi_{2i}$
		ϕ_{1i}	ϕ_{2i}	
0[a]	0	1	1	1
12.02	75.52	$-0.172\ 10^{-6}$	$-0.137\ 10^{-6}$	$0.0236\ 10^{-12}$
12.58[a]	79.04	$0.126\ 10^{-2}$	$0.984\ 10^{-3}$	$0.1240\ 10^{-5}$
34.48[a]	216.6	$0.141\ 10^{-1}$	$-0.123\ 10^{-2}$	$-1.7300\ 10^{-5}$
53.90	338.7	$-0.414\ 10^{-7}$	$0.754\ 10^{-8}$	$-0.3121\ 10^{-15}$
55.29[a]	347.4	$0.343\ 10^{-2}$	$-0.604\ 10^{-3}$	$-0.2070\ 10^{-5}$
67.62[a]	424.9	$0.578\ 10^{-2}$	$0.139\ 10^{-2}$	$0.8030\ 10^{-5}$
79.82[a]	501.5	$0.152\ 10^{-2}$	$-0.825\ 10^{-3}$	$-0.1250\ 10^{-5}$
80.46[a]	505.5	$-0.467\ 10^{-2}$	$-0.138\ 10^{-2}$	$0.6400\ 10^{-5}$
110.62[a]	695.0	$-0.415\ 10^{-2}$	$0.132\ 10^{-2}$	$-0.5480\ 10^{-5}$
147.18[a]	924.8	$0.163\ 10^{-2}$	$-0.855\ 10^{-3}$	$-0.1394\ 10^{-5}$

[a] Selected modes.
Note: $m_i = 1.0$, $i = 1, 2, \cdots$; $m_0 = 105{,}400$ lb-in.-sec^2.

modes. Substitution of the numerical value of Table B-1 into Eqs. (1), (5), and (6) leads to Eqs. (7) through (16).

B. Atlas/Centaur/Surveyor

The dynamic torsional model corresponding to the *Atlas/Centaur/Surveyor* is a 66-degree-of-freedom spring mass system (Ref. 2).

The first 27 normal modes are shown in Table B-2. Only 16 modes were retained; the selection was based on the product $\phi_{0i}\,\phi_{2i}$. All modes for which the product $\phi_{0i}\,\phi_{2i}$ is smaller than $0.2\ 10^{-6}$ have been discarded. Substitution of the numerical values corresponding to these 15 modes into Eqs. (18) and (19) leads to Eqs. (20) through (35).

Table B-2. Normal modes for *Atlas/Centaur/Surveyor*

f_i, cps	ω_i, rad/sec	Joint 16 Field joint	Joint 26 Gimbal block	$\phi_{2i}\,\phi_{0i}$
		ϕ_{0i}	ϕ_{2i}	
0[a]	0			
8.45	53.09	$0.32393\ 10^{-5}$	$-0.43615\ 10^{-6}$	$-0.14128\ 10^{-10}$
11.74[a]	73.76	$0.10840\ 10^{-2}$	$-0.23721\ 10^{-3}$	$-0.25714\ 10^{-6}$
12.01	75.47	$0.33197\ 10^{-7}$	$0.15829\ 10^{-8}$	$0.52547\ 10^{-16}$
12.17[a]	76.44	$0.95338\ 10^{-3}$	$0.21914\ 10^{-3}$	$0.20892\ 10^{-6}$
12.54	78.76	$0.30693\ 10^{-8}$	$-0.56252\ 10^{-9}$	$-0.17265\ 10^{-17}$
14.22[a]	89.36	$0.38167\ 10^{-3}$	$-0.75921\ 10^{-3}$	$-0.28977\ 10^{-6}$
16.80[a]	105.5	$0.81889\ 10^{-3}$	$-0.44056\ 10^{-3}$	$-0.36077\ 10^{-6}$
16.98[a]	106.7	$0.35791\ 10^{-2}$	$-0.19327\ 10^{-2}$	$-0.69173\ 10^{-6}$
23.58	148.2	$0.15257\ 10^{-4}$	$0.34364\ 10^{-4}$	$0.52429\ 10^{-9}$
35.81	225.0	$0.47065\ 10^{-3}$	$0.46710\ 10^{-4}$	$0.21984\ 10^{-7}$
38.78	243.6	$0.14301\ 10^{-3}$	$0.13196\ 10^{-4}$	$0.18871\ 10^{-8}$
45.43[a]	285.5	$0.49796\ 10^{-2}$	$0.80271\ 10^{-3}$	$0.39972\ 10^{-6}$
48.07	302.0	$-0.20366\ 10^{-4}$	$-0.16443\ 10^{-4}$	$0.33488\ 10^{-9}$
51.77	325.3	$0.19141\ 10^{-3}$	$-0.17316\ 10^{-4}$	$-0.33145\ 10^{-8}$
54.35[a]	341.5	$-0.16377\ 10^{-2}$	$-0.22556\ 10^{-3}$	$0.36940\ 10^{-6}$
55.54	349.0	$-0.17567\ 10^{-8}$	$-0.17029\ 10^{-9}$	$0.29915\ 10^{-18}$
57.36	360.4	$0.18347\ 10^{-3}$	$-0.10780\ 10^{-4}$	$-0.19778\ 10^{-8}$
57.98	364.3	$0.15627\ 10^{-3}$	$-0.55802\ 10^{-6}$	$-0.87202\ 10^{-9}$
67.50[a]	424.1	$0.51868\ 10^{-3}$	$-0.21188\ 10^{-2}$	$-0.10990\ 10^{-5}$
70.19[a]	441.0	$0.13474\ 10^{-1}$	$-0.20455\ 10^{-3}$	$-0.27561\ 10^{-5}$
79.97	502.5	$0.93115\ 10^{-4}$	$-0.12717\ 10^{-2}$	$-0.11841\ 10^{-6}$
96.60[a]	606.9	$-0.82726\ 10^{-2}$	$-0.59479\ 10^{-3}$	$0.49204\ 10^{-5}$
110.0[a]	691.2	$0.50664\ 10^{-2}$	$-0.79742\ 10^{-3}$	$-0.40400\ 10^{-6}$
130.0[a]	816.8	$-0.15283\ 10^{-2}$	$0.73311\ 10^{-3}$	$-0.11204\ 10^{-5}$
132.6[a]	833.4	$-0.21674\ 10^{-2}$	$-0.76145\ 10^{-3}$	$0.16504\ 10^{-6}$
145.0[a]	911.1	$-0.85950\ 10^{-2}$	$-0.26403\ 10^{-3}$	$0.22693\ 10^{-6}$
158.1[a]	993.4	$-0.34112\ 10^{-2}$	$0.94587\ 10^{-3}$	$-0.82265\ 10^{-6}$

[a] Selected modes.

Note: $m_i = 1.0, (i = 1, 2, \cdots, 9)$; $m_0 = 185{,}000$ lb-in.-sec^2.

APPENDIX C

Coefficients for Synthesized Pulses $\ddot{\theta}_2$

$$\ddot{\theta}_2 = t \sum_{i=1}^{n} a_i e^{-\beta_i t} \sin 2\pi f_i t \qquad (\text{rad/sec}^2)$$

Flight	f_i, cps	a_i, rad/sec^3	β_i,
Ranger VI	8	−24.45	20.6
	20	−24.45	14.6
	47	−40.75	20.6
	67	−97.80	14.6
	85	48.90	26.6
	95	−130.40	17.8
Ranger VII	8	−40.0	20.2
	20	18.0	20.2
	31	10.0	20.2
	51	95.0	20.2
	64	35.0	20.2
	72	20.0	20.2
	82	70.0	20.2
	96	90.0	20.2
	113	70.0	20.2
Ranger VIII	20	100.0	40.6
	38	−60.0	12.7
	43	−105.2	11.2
	50	144.0	14.4
	61	36.0	19.1
	71	300.0	19.2
	90	560.0	40.6
Ranger IX	12	−20.5	22.2
	24	16.4	19.0
	37	−24.6	15.9
	53	61.5	15.9
	68	51.25	14.6
	94	65.6	28.7

APPENDIX D

Derivation of Eqs. (36), (37), and (38)

A. Structural System

Here again, it is most convenient to express the dynamic characteristics of the spacecraft by means of the normal modes (Fig. D-1). The cantilevered configuration (i.e., the spacecraft rigidly mounted on its base) has been chosen here for convenience. The upper part of the adapter was taken as an integral element of the spacecraft, the field joint becoming the fixed station. We first write the matrix equation representing the free vibration of the structure, viz.,

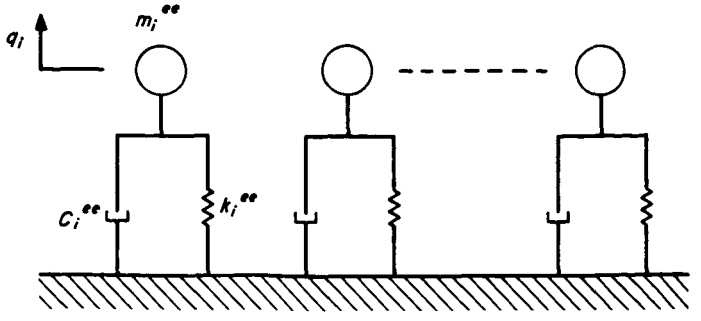

Fig. D-1. Schematic representation of cantilevered spacecraft by its normal modes

$$[M^{ee}]\{\ddot{q}\} + [C^{ee}]\{\dot{q}\} + [K^{ee}]\{q\} = 0, \qquad \text{(D-1)}$$

in which $[M^{ee}]$ is the diagonal generalized mass matrix; $[C^{ee}]$ is the diagonal generalized damping matrix; $[K^{ee}]$ is the diagonal generalized stiffness matrix; and $\{q\}$ is the column of the generalized coordinates relative to the base.

Then the spacecraft is mounted on the shake table (Fig. D-2) and a base rotation θ_0 is allowed to take place,

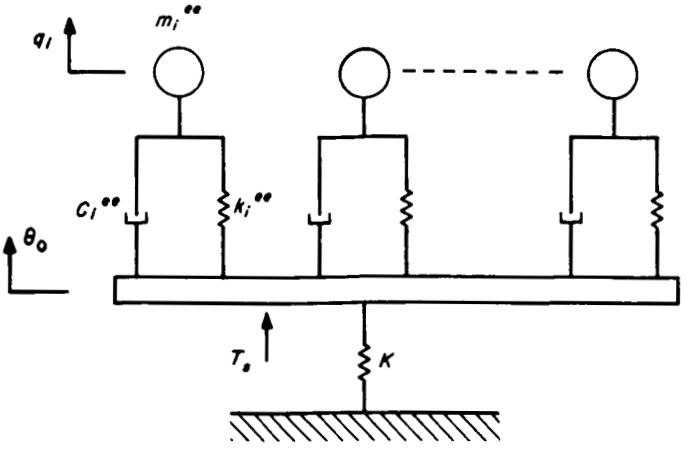

Fig. D-2. Schematic representation of spacecraft mounted on shake table

giving an unrestrained free system. The equations of motion are (Ref. 6):

$$\begin{bmatrix} M^{rr} & M^{re} \\ M^{er} & M^{ee} \end{bmatrix} \begin{Bmatrix} \ddot{\theta}_0 \\ \ddot{q} \end{Bmatrix} + \begin{bmatrix} 0 & 0 \\ 0 & C^{ee} \end{bmatrix} \begin{Bmatrix} \dot{\theta}_0 \\ \dot{q} \end{Bmatrix} + \begin{bmatrix} 0 & 0 \\ 0 & K^{ee} \end{bmatrix} \begin{Bmatrix} \theta_0 \\ q \end{Bmatrix} = 0 \tag{D-2}$$

where M^{rr} is the total moment of inertia of the spacecraft and all the moving parts of the shake table, $\{M^{er}\}$ is a column representing the coupling between the elastic modes and the rigid body rotation, and the row $\langle M^{re} \rangle$ is the transpose of the column $\{M^{er}\}$.

It is recalled that the terms of the column $\{M^{er}\}$ are

$$m_n^{er} = \sum_i m_i \phi_{in} \tag{D-3}$$

where ϕ_{in} is the modal displacement of the i^{th} mass m_i in the n^{th} cantilever mode.

Finally an external torque T_s is applied on the base by means of the armature of the shakers, which also provide a stiffness k between the table and the ground (Figs. D-3 and D-4). The forcing function corresponding to the base rotation θ_0 is

$$F_s = T_s - K\theta_0, \tag{D-4}$$

with

$$K = 3kl^2, \tag{D-5}$$

where l is the distance from the axis of rotation to the shakers (Fig. D-3). All other generalized forces corresponding to the coordinates $\{q\}$ being zero, the matrix equation of motion for the forced vibration of the system is:

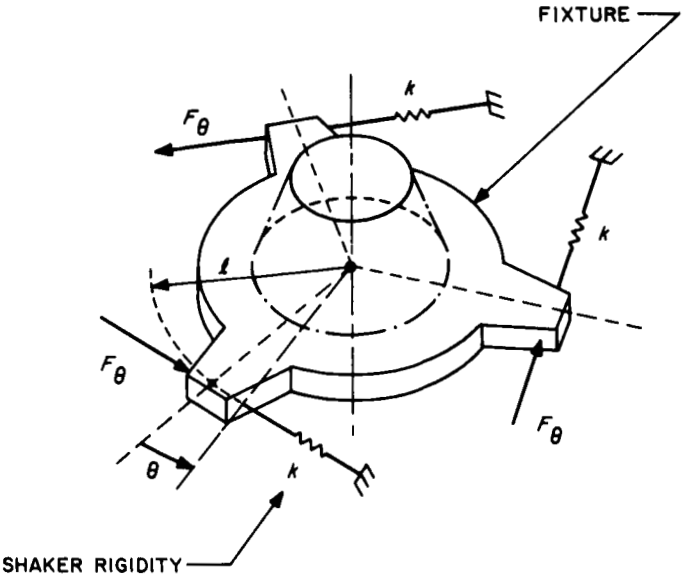

Fig. D-3. Schematic mounting of shakers on fixture

$$\begin{bmatrix} M^{rr} & M^{re} \\ M^{er} & M^{ee} \end{bmatrix} \begin{Bmatrix} \ddot{\theta}_0 \\ \ddot{q} \end{Bmatrix} + \begin{bmatrix} 0 & 0 \\ 0 & C^{ee} \end{bmatrix} \begin{Bmatrix} \dot{\theta}_0 \\ \dot{q} \end{Bmatrix} + \begin{bmatrix} 0 & 0 \\ 0 & K^{ee} \end{bmatrix} \begin{Bmatrix} \theta_0 \\ q \end{Bmatrix} = \begin{Bmatrix} T_s - K\theta_0 \\ 0 \end{Bmatrix} \tag{D-6}$$

B. Electrodynamic Equations

The torque T_s is applied by means of three identical shakers placed 120° apart around the base of the spacecraft (Fig. D-3). We have:

$$T_s = 3l\lambda i \tag{D-7}$$

where i is the armature current; λ is the force/current coefficient; and l is the distance from the axis of rotation.

The three shakers are electrically connected in series; therefore, Ohm's law, corrected for the back electromotive force $\lambda l\dot{\theta}_0$ due the armature motion is:

$$e = 3Ri + 3L\frac{di}{dt} + 3\lambda l\dot{\theta}_0, \tag{D-8}$$

where R is the electrical resistance of each armature; L is the armature self-inductance; and e is the total voltage applied by the power amplifier on the armatures (Fig. D-5).

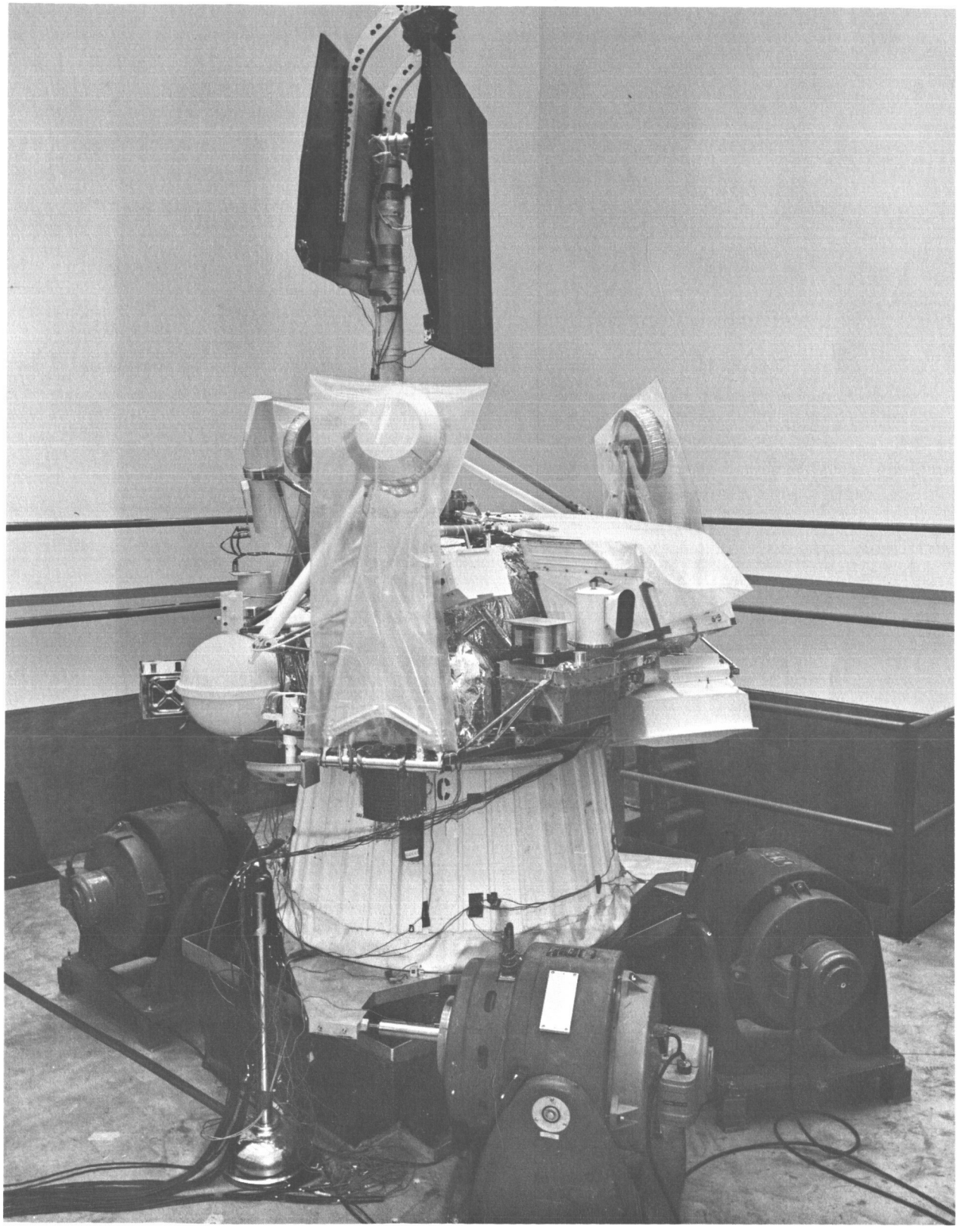

Fig. D-4. Testing assembly

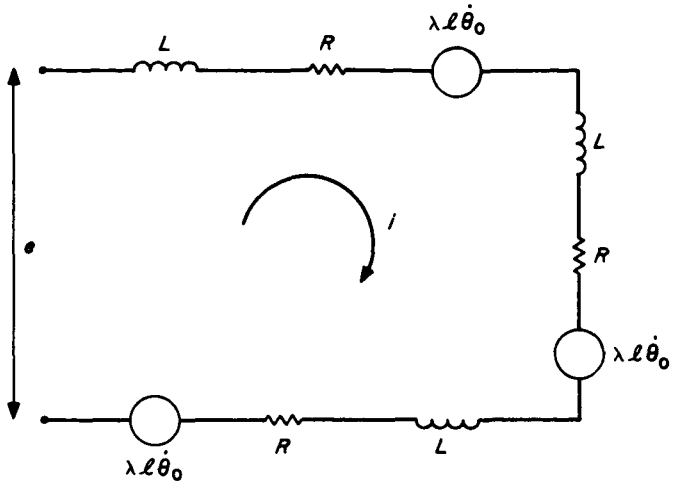

Fig. D-5. Series circuit for armatures

Expanding Eq. (D-6) and eliminating i between (D-7) and (D-8), we obtain Eqs. (36), (37), and (38).

C. Numerical Values

The nominal electromechanical characteristics of the shakers are: (Ref. 7)

Force current coefficient	$\lambda = 30.20$ lb/amp $= 134.5$ newton/amp
Weight	$w = 17.5$ lb
Mass	$m = 7.935$ kg
Resistance	$R = 3$ ohm
Inductance	$L = 0.012$ henry
Rigidity	$k = 360$ lb/in. $= 63{,}000$ newton/m
Distance from axis	$l = 42$ in. $= 1.068$ m

The metric system of units (MKSA) has been used here in parallel with the British system because the former is the most convenient for electromechanical problems. However, the MKSA system was used only as an intermediate step; the torque T_s in Eqs. (48) and (49) has been reconverted in inch-pounds for ease of interpretation. The total mass moment of inertia M^{rr} is:

$$M^{rr} = 3575 \text{ lb-in.-sec}^2.$$

The breakdown of this M^{rr} is:

Components	Pound-inch-second^2
Spacecraft	2199
Armature	240
Connecting rod	211
Plate slider	85
Fixture	840
	3575

The matrices $[M^{ee}]$, $[C^{ee}]$, $[K^{ee}]$, and $\{M^{er}\}$ are:

$$[M^{ee}] = \begin{bmatrix} 1 & 0 & 0 & 0 & 0 & 0 & 0 & 0 & 0 \\ 0 & 1 & 0 & 0 & 0 & 0 & 0 & 0 & 0 \\ 0 & 0 & 1 & 0 & 0 & 0 & 0 & 0 & 0 \\ 0 & 0 & 0 & 1 & 0 & 0 & 0 & 0 & 0 \\ 0 & 0 & 0 & 0 & 1 & 0 & 0 & 0 & 0 \\ 0 & 0 & 0 & 0 & 0 & 1 & 0 & 0 & 0 \\ 0 & 0 & 0 & 0 & 0 & 0 & 1 & 0 & 0 \\ 0 & 0 & 0 & 0 & 0 & 0 & 0 & 1 & 0 \\ 0 & 0 & 0 & 0 & 0 & 0 & 0 & 0 & 1 \end{bmatrix}$$

$$[C^{ee}] = \begin{bmatrix} 2.12 & 0 & 0 & 0 & 0 & 0 & 0 & 0 & 0 \\ 0 & 7.20 & 0 & 0 & 0 & 0 & 0 & 0 & 0 \\ 0 & 0 & 12.9 & 0 & 0 & 0 & 0 & 0 & 0 \\ 0 & 0 & 0 & 16.1 & 0 & 0 & 0 & 0 & 0 \\ 0 & 0 & 0 & 0 & 23.0 & 0 & 0 & 0 & 0 \\ 0 & 0 & 0 & 0 & 0 & 20.1 & 0 & 0 & 0 \\ 0 & 0 & 0 & 0 & 0 & 0 & 26.0 & 0 & 0 \\ 0 & 0 & 0 & 0 & 0 & 0 & 0 & 28.8 & 0 \\ 0 & 0 & 0 & 0 & 0 & 0 & 0 & 0 & 30.0 \end{bmatrix}$$

$$[K^{ee}] = \begin{bmatrix} 2818.5 & 0 & 0 & 0 & 0 & 0 & 0 & 0 & 0 \\ 0 & 14{,}200 & 0 & 0 & 0 & 0 & 0 & 0 & 0 \\ 0 & 0 & 25{,}600 & 0 & 0 & 0 & 0 & 0 & 0 \\ 0 & 0 & 0 & 40{,}400 & 0 & 0 & 0 & 0 & 0 \\ 0 & 0 & 0 & 0 & 51{,}000 & 0 & 0 & 0 & 0 \\ 0 & 0 & 0 & 0 & 0 & 60{,}310 & 0 & 0 & 0 \\ 0 & 0 & 0 & 0 & 0 & 0 & 105{,}930 & 0 & 0 \\ 0 & 0 & 0 & 0 & 0 & 0 & 0 & 130{,}104 & 0 \\ 0 & 0 & 0 & 0 & 0 & 0 & 0 & 0 & 142{,}121 \end{bmatrix}$$

$$\{M^{er}\} = \begin{Bmatrix} -5.5 \\ -27.7 \\ -17.3 \\ -15.0 \\ -12.5 \\ -10.9 \\ -6.5 \\ -0.58 \\ -0.34 \end{Bmatrix}$$

When substituted into Eqs. (36), (37), and (39), all of the previous numerical values give the set of equations (39) through (49).

REFERENCES

1. Howard, J. D., "Beco and SECO Transient Oscillation for SLV-3 Vehicles," General Dynamics/Convair Report No. GD/C-DDE 65-068 (to be published).
2. Garba, J. A., Gayman, W. H., and Wada, B., *Computation of Torsional Vibration Modes of Ranger and Surveyor Space Vehicles*, Technical Memorandum No. 33-277, Jet Propulsion Laboratory, Pasadena, California (to be published).
3. Rogers, G. L.; *Dynamics of Framed Structures*, p. 145, John Wiley & Sons, New York, 1959.
4. Hurty, W. C., and Rubinstein, M. F., *Dynamics of Structures*, p. 285, Prentice-Hall, 1964.

REFERENCES (Cont'd)

5. Hendrich, W. R., and Harter, R. J., *Revised Mathematical Model of the Surveyor Mounted on the GD/A Adapter*, Hughes Aircraft Company, Report 2222.4/9, July 23, 1964.

6. Hurty, W. C., *Dynamic Analysis of Structural Systems by Component Mode Synthesis*, Technical Report No. 32-530, Jet Propulsion Laboratory, Pasadena, California, 1964.

7. Private communication from the Environmental and Dynamic Testing Section, JPL.

ACKNOWLEDGEMENT

This investigation was conducted with the collaboration of W. H. Gayman, Assistant Manager of the Applied Mechanics Section of the Jet Propulsion Laboratory, and J. A. Garba and B. Wada, Senior Engineers in the Applied Mechanics Section, who derived the mathematical models for all the structures. (See Ref. 2.)

The author is also indebted to Dr. M. E. Alper, Manager of the Jet Propulsion Laboratory's Applied Mechanics Section, for his constant encouragement during this investigation, to R. E. Freeland, Senior Engineer of the same section, who made the hardware test possible, and to G. E. Fleischer, of the Data Systems Section's Analog Computer Facility, who conducted the analog programming and computation. Thanks are also extended to the personnel of the other sections of the Jet Propulsion Laboratory for their invaluable help during the course of this work. Special mention is made to the Environmental Requirements Section, the Environmental and Dynamic Testing Section, and the Data Analysis Laboratory of the Data Systems Section.